Development of VO_2-based tunable micro-resonators

by

Emmanuelle J Merced-Grafals

A thesis submitted in partial fulfillment of the requirements for the degree of

MASTER OF SCIENCE
in
ELECTRICAL ENGINEERING

UNIVERSITY OF PUERTO RICO
MAYAGÜEZ CAMPUS
2011

Approved by:

Nelson Sepulveda-Alancastro, PhD President, Graduate Committee	Date
Félix E. Fernández, PhD Member, Graduate Committee	Date
Manuel Toledo-Quiñones, PhD Member, Graduate Committee	Date
Erick Aponte, PhD Chairperson of the Department	Date
Omar Colón-Reyes, PhD Graduate School Representative	Date

ABSTRACT

This work presents the development of a tunable micro-mechanical resonator capable of reaching resonant frequency shifts of 23%. The resonator consists of a simple SiO_2 bridge, which was fabricated using standard micro-fabrication technologies and then coated with a thin film of vanadium dioxide (VO_2). The VO_2 film was deposited by pulsed-laser-deposition (PLD). VO_2 undergoes an insulator-to-metal transition (IMT) at close-to-room temperatures (~65°C). The observed frequency shift is due to the large stress levels that are induced on the bimorph structure due to the contraction of the VO_2 film during the IMT. The simultaneous characterization of the VO_2 film resistance and the resonant frequency of the bimorph micro-bridge structures coated with VO_2 is accomplished using heating by conduction and by light irradiation. Both methods are compared. A temperature-to-laser-intensity relationship is also found and discussed along with a finite element method (FEM) analysis of the temperature distribution in the micro-bridge.

RESUMEN

Este trabajo presenta el desarrollo de un micro-resonador sintonizable capaz de alcanzar hasta un 23% en cambios de frecuencia de resonancia. El resonador consiste de un simple puente de SiO_2, que fue fabricado usando tecnologías convencionales de micro-fabricación, recubierto de una fina capa de dióxido de vanadio (VO_2), la cual fue depositada mediante láser pulsado (PLD). El VO_2 atraviesa una transición de aislante a metal (IMT) en función de temperatura cercana a ambiente (~ 65 °C). El cambio de la frecuencia se debe a los niveles de estrés que se inducen en la estructura bimorfa debido a la contracción de la película de VO_2 durante el IMT. La caracterización simultánea de la resistencia de la película de VO_2 y la frecuencia de resonancia de los micro-puentes cubiertos con VO_2 fue realizada mediante calentamiento por conducción y por irradiación de luz. Ambos métodos son comparados y se encuentra una relación entre la temperatura y la intensidad del laser. Para validar los datos obtenidos y la diferencia entre ambos métodos de actuación, se simula la transferencia de calor en el dispositivo utilizando un método de elementos finitos (FEM).

To my family and Fiancée . . .

ACKNOWLEDGEMENTS

During the course of my graduate studies in the University of Puerto Rico at Mayagüez, several persons and organizations collaborated with my research. Without their support it would have been impossible for me to finish my research.

I want to express my sincere acknowledgement to my advisor, Dr. Nelson Sepúlveda-Alancastro since he gave me the opportunity to do research under his guidance and supervision. I received inspiration and support from him during all my studies and my research work. Most importantly, we created a bond and a friendship that has helped us in our personal and academic lives.

I also want to thank the knowledge and support I received from Dr. Félix Fernández. He was an indispensable member of my graduate committee and our research group. I owe special thanks to Dr. Manuel Toledo for his enthusiasm and interest in my research topic and his ideas for future work. I give special thanks to Rafmag Cabrera whose research experience and knowledge had also helped me overcome obstacles and difficulties in my work.

I would also like to thank my father, mother, brother and grandmother. It was their help, support and motivation that guided me through my graduate studies.

Finally, I specially thank Noraica Dávila, my fiancée, for the support, patience, motivation and unconditional love she provided me throughout my research and thesis writing even in the days I retreated to the computer.

This work was supported in part by the National Science Foundation under Grants No. HRD 0833112 (CREST Program) and No. ECCS-0954406 (CAREER Program).

Table of Contents

ABSTRACT .... **II**

RESUMEN .... **III**

ACKNOWLEDGEMENTS .... **V**

TABLE OF CONTENTS .... **VI**

FIGURE LIST .... **I**

1 INTRODUCTION **2**

1.1 RATIONALE 2
1.2 LITERATURE REVIEW 4
1.2.1 VO_2 Insulator-To-Metal Transition and Characterization *4*
1.2.2 Electrical Circuits Applications *5*
1.2.3 Hysteresis Modeling of VO_2 Transition *7*
1.3 ORGANIZATION OF THIS DOCUMENT 8

2 THEORETICAL BACKGROUND **9**

2.1 RESONATORS 9
2.1.1 Electrical Resonance *10*
2.1.2 Mechanical Resonance *12*
2.2 MICRO-BRIDGE MECHANICAL BEHAVIOR 14
2.2.1 Transverse Vibrations *14*
2.2.2 Resonant Frequency of Unbuckled Bridges *16*
2.2.3 Euler Buckling Limit *16*
2.2.4 Resonant Frequency of Bukled Bridges *18*
2.2.5 Bilayer Bridge *20*
2.3 TEMPERATURE COEFFICIENT OF RESISTIVITY 22
2.4 JUSTIFICATION 23

3 MATERIALS AND METHODS **26**

3.1 SiO_2 MICRO-RESONATORS AND VO_2 DEPOSITION 26
3.2 MEASUREMENT SYSTEM AND PROCEDURE 28

4 RESULTS AND ANALYSIS **34**

4.1 SIMULTANEOUS RESONANT FREQUENCY AND ELECTRICAL RESISTANCE 34
4.1.1 Conduction Method *34*
4.1.2 Uncoated vs. Coated Bridge Resonant Frequency *36*
4.1.3 Resistance and Resonant Frequency Curves *39*
4.1.4 VO_2-coated SiO_2 cantilever *41*
4.1.5 Irradiation Method *43*
4.1.6 Comparison Between Actuation Methods *46*
4.2 RESISTIVITY AND TCR 52

5 CONCLUSIONS AND FUTURE WORK **58**

5.1 CONCLUSION 58
5.2 FUTURE WORK 59

Figure List

Figures **Page**

Figure 2.1 – a) Location of complex poles for a resonator, and b) resonant frequency curve. 9
Figure 2.2 – RLC band-pass filter. 11
Figure 2.3 – Tunable capacitor. 12
Figure 2.4 – Mechanical system elements and their respective electrical analogs. 13
Figure 2.5 – Micro-bridge structure. 14
Figure 2.6 – Buckled micro-bridge. 18
Figure 2.7 – Resonant frequency bridge as a function of axial stress for the unbuckled (red) and buckled (blue) state. 20
Figure 3.1 – Top view of the released micro-bridges. 26
Figure 3.2 – A-A’ cross-sectional view of the VO_2 coated MEMS resonator. 27
Figure 3.3 – Picture of the VO_2 coated micro-bridge. 28
Figure 3.4 – Schematic of the simultaneous resistance and frequency measurements setup. 29
Figure 3.5 – Picture of the resonant frequency and resistance measurement setup. 30
Figure 4.1 –Resistance (a) and resonant frequency (b) of the micro bridge as a function of temperature through the IMT for the *conduction method*. 35
Figure 4.2 – Resonant frequency as a function of temperature for bare and VO_2-coated SiO_2 bridges. 37
Figure 4.3 – Resonant frequency as a function of temperature for a 200 μm long VO_2-coated SiO_2 micro cantilever (*for conduction method*). 42
Figure 4.4 – Optical power calibration as a function of the current supplied to the diode (a) and sample temperature measured with the thermocouple as a function of optical power density on the sample (b). 44
Figure 4.5 – Resistance (a) and resonant frequency (b) of the micro bridges as a function of temperature thru the IMT for the *irradiation method*. 45
Figure 4.6 – Comparison between the two heating methods, conduction and irradiation for the resistance (a) and resonant frequency (b) change as a function of temperature. 47
Figure 4.7 – Geometry of the micro-resonator simulated in COMSOL. The inset shows the VO_2 coated SiO_2 micro-bridge more clearly. Under-etching effects were considered. 48
Figure 4.8 – Thermal properties of the materials simulated in COMSOL. 49
Figure 4.9 – Average temperature at the bridge and thermocouple boundary as a function of inflow heat flux for the simulated *conduction* (a) and *irradiation* (b) *methods*. 50
Figure 4.10 – Temperature as a function of bridge length for the simulated *conduction* (a) and *irradiation* (b) *methods*. 51
Figure 4.11 – Setup for resistivity calculation using optical radiation and conductive heating with the three parallel bridges and one bridge experiments. The bridges are numbered from 1to 3. 52
Figure 4.12 – Calculated resistivity as a function of delivered optical power (a) and temperature (b) for heating-cooling cycles for the conduction (2 curves with “x” symbol), and irradiation methods (2 curves with “●” symbol). 55
Figure 4.13 – Calculated TCR as a function of delivered optical power (a) and temperature (b) for heating-cooling cycles for the conduction (2 curves with “x” symbol), and *irradiation methods* (2 curves with “●” symbol). 57
Figure A.1 – The Preisach hysteron. 60
Figure A.2 – The discretized Preisach operator. 61
Figure A.3 – Preisach operator operational principle. 62
Figure A.4 – Discretized Preisach output block model with weighting functions. 63
Figure A.5 – Inversion block diagram. 64
Figure A.6 – VO_2 resistance control scheme. 65
Figure A.7 – Block diagram of dynamic model for controlled VO_2 hysteresis. 66

1 INTRODUCTION

1.1 RATIONALE

For many decades researchers have studied the insulator-to-metal transition (IMT) of VO_2 in thin films which undergoes a solid-to-solid phase transition. Such transition, when thermally induced, occurs at close-to-room temperatures (~68˚C) [1]. During this transition the electrical [1], structural [2] and optical properties [3] of the material change abruptly as a function of temperature following a hysteresis behavior. It has been shown that this VO_2 transition can be induced by ultrafast optical radiation [3], by electrical signals [4], by direct heating and by pressure change [5].

The use of VO_2 thin film is currently being considered in solid-state-based tunable frequency resonators [6] and filters [7], and memristors [8], whereas its use in MEMS has been limited. However, recent results have demonstrated a drastic change on the mechanical properties of VO_2 films during its IMT [9], giving an extra functionality to VO_2 films that could be very beneficial for the development of MEMS-based transducers.

This work addresses the characterization of VO_2-coated SiO_2 micro-mechanical bridges by simultaneously measuring their change in resonant frequency and the VO_2 film resistance due to ordinary heating by conduction or by optical radiation. In addition, there has been no reported work on the characterization of VO_2 films deposited on SiO_2 bridges, which can be of great importance in circuits because of its insulating properties. It should be mentioned, however, that previous work on V_6O_{13} films on SiO_2 cantilevers has been

reported [10], but this mixed valence vanadium oxide shows a transition at very low temperatures (~ 50 K), which is not practical for most applications.

In a monolithically integrated MEMS, the heating by direct conduction would require the inclusion of a micro-heater in the MEMS design. The increase in temperature generated by these micro-heaters is caused by an electrical current flowing through a micro-meter sized conductive line (*i.e.* Joule heating) [11,12]. Due to the compact nature of many MEMS designs, it is sometimes difficult to account for heating undesired elements of the MEMS device, even when thermal insulating layers are included. Therefore, micro-heaters make the whole MEMS design more complicated and expensive. The use of optical radiation for the thermal tuning of oscillators and filters eliminates the need of these micro-heaters by allowing for localized temperature increases that can be provided remotely. This work explores these two thermal actuation methods: optical radiation and conduction.

Other steps towards the characterization of our system are: 1. to determine the resonant frequency full scale operating range of the bimorph micro-bridge hysteresis system, 2. to find the relationship between optical power density delivered to the device and its temperature, 3. to determine the temperature coefficient of resistivity (TCR) of the VO_2 film as a function of temperature, 4. the simulation of the temperature distribution along the micro-bridge by using a finite element method (FEM) software, and 5. to present a preliminary study of nonlinear control theory for VO_2 hysteresis. This last task is essential to the future design, implementation, and validation of control theories that will ensure the system operation in the IMT region desired values. This characterization will then be used to simulate and test VO_2-based circuits and devices.

1.2 LITERATURE REVIEW

1.2.1 VO_2 Insulator-To-Metal Transition and Characterization

VO_2 transition was first discovered and documented by F. J. Morin [1] who studied the resistance, heat capacity and magnetic susceptibility change of VO_2 as a function of temperature. A reduction of more than two orders of magnitude in the resistance of the crystals was observed with hysteresis behavior. He explained the transition as a competition of two processes: 1) A correlation effect that localizes the electrons and sets their spin in an antiferromagnetic alignment and 2) An effect in which electrons gain kinetic energy delocalizing themselves. It was then concluded that a split upper empty and lower full levels of a partially filled band describes the transition. These lower full levels have localized electrons with an antiferromagnetic alignment.

G. Rozgonyi *et al*. studied VO_2 thin films deposited in different types of substrates including glass, glazed ceramic, sapphire and rutile [2]. It was concluded that VO_2 thin films deposited on glass and ceramics have transition magnitudes lower than those deposited on sapphire and rutile, which have a reduction of more than four orders of magnitude. It was also observed that the substrate also influenced the hysteresis width as well as the transition temperature. It was determined that other factors influenced the hysteresis width and transition temperature; such as deposition techniques and parameters, doping, and annealing conditions. These factors also affected the grain size, the residual internal stresses, and the stoichiometry of VO_2 films.

Recent studies describe the IMT in VO_2 films as a combination of two phenomena: 1) the movement of the atoms inside the unit cell and 2) the lattice organization [13]. Before the transition, the atomic structure of VO_2 is described as a monoclinic phase and after the transition it is described as a tetragonal phase. Infrared imaging has been used to demonstrate that the transition from insulator to metal in VO_2 is of the form of nanoscale puddles, where metallic and insulator phases coexist over the finite temperature range in the transition [14].

There are a handful of studies in the mechanical behavior of silicon micro-cantilevers coated with VO_2 [9], [15]. These studies describe the pulsed laser deposition (PLD) technique used to deposit the VO_2 thin films and the effects of the deposition parameters on the film composition and mechanical properties. It was found that, during the transition, the coated micro-cantilevers could increase their resonant frequency by ~5% [15] and their total bending could reach a radius of curvature change of 2000 m^{-1} [16]. In [17], it was found that for very thin VO_2 film coatings (~35 nm) on silicon cantilevers, the bimorph cantilever bending across the IMT was minimal, and the frequency shifts of ~1% were used to calculate the Young's modulus of the thin film tested.

1.2.2 Electrical Circuits Applications

The results mentioned above demonstrate that the VO_2 characteristic behavior across the IMT can produce changes in the resonant frequency and electrical resistance of the micro-mechanical structure with which it is integrated in the form of film coating. These changes could be used to develop tunable electrical devices and MEMS. So far, only the

drastic change in the resistivity of VO_2 films has been exploited in solid-state-based tunable resonators and filters, field effect transistors, and in the recently demonstrated memristor.

1.2.2.1 Tuning resonators and filters

Researchers in the area of solid-state-based tunable resonators and filters are gaining interest in the use of VO_2 for new devices. A novel design of a VO_2-based tunable band stop filter was tested and validated [7]. The new system aims at substituting the current devices, which consist of power consuming amplifiers and non-linear semiconductor components. The device takes advantage of the large resistance change in the IMT in order to reject a non-desired signal. By using voltage pulses to modify the resistance that switched on and off one or more resonators, the rejection band of the filter can be eliminated from the frequency range or it can be tuned to other frequency bands.

The device in reference [18] is a reconfigurable bandpass filter based on split ring resonators with VO_2 microwave switches. It uses the resistance change through the IMT in order to change the resonant frequency of the 4-bit tunable filter. With this design, the device is able to move the pass band cut-off frequencies in order to modify the bandwidth location.

The three devices tested in reference [18] showed split ring resonator devices with different geometries coated with VO_2. The frequency responses for all three geometries changed as the IMT (induced by thermal conduction) took place.

1.2.2.2 Memristors

Leon Chua theoretically conceived the memristor in 1971 [19], but it wasn't until recently, that it was physically tested and implemented using TiO_2 [20]. The memristor has been previously modeled as two variable resistors connected in series and one of the resistor changed with an applied voltage [20]. As discussed previously, during the IMT, if the hysteresis is wide enough, different states can be achieved and "saved" in the thin film.

T. Driscoll *et al*. presented the first studies on VO_2-based memristors [8]. They demonstrated the memristive behavior of the electrical resistance of VO_2 films across its IMT. Using voltage pulses only (no changes in temperature), the resistance values between two contacts in the VO_2 film were changed and these values remained for long periods of time with no further stimulus. It was concluded that the memristance is directly related to the power dissipated in VO_2. By applying a voltage pulse signal, very small resistance steps can be achieved which could yield a lot more than 2^{10} resistance values.

The memory effect is not limited only to electrical resistance. An electrically controlled frequency tuning material has also been presented [21]. The device presented is a hybrid design made of a resonant metamaterial and VO_2. By applying an excitation voltage to the VO_2, a change in its permittivity produces a change in the resonant frequency which changes the capacitance value of RLC circuit. In other words, VO_2 is used to create a capacitance memory by changing the permittivity across the IMT region.

1.2.3 Hysteresis Modeling of VO_2 Transition

One important step in order to find and simulate the different system responses is to find the mathematical model that represents, in this case, the hysteresis behavior of the IMT

in VO_2 thin films. Many techniques have been implemented in order to model this type of behavior which include: Boltzmann models, the Preisach operator models, and resistor network models.

The Boltzmann model approach reported previously, involves a sigmoid function which depends on the experimental data [9]. This sigmoid may or may not be used for temperature range depending on the hysteresis behavior. A more complete model of the hysteresis behavior found in VO_2 was found by using the Preisach operator model [22]. Although mathematically challenging, it holds the highest correlation between the experimental data and simulation, as can be found in the reference results. Another method used in [23] is the random resistor network in which the hysteresis system is modeled as a binary medium of random distribution representing the metallic and semiconductor regions in VO_2.

1.3 ORGANIZATION OF THIS DOCUMENT

In Chapter 2 of this thesis, the necessary background theory for understanding the problem and results is discussed. Chapter 3 presents the methodology for the characterization of the VO_2-coated SiO_2 micro-bridges including the setup for the simultaneous measurement of resistance and resonant frequency and the methods for calculating resistivity and the TCR as a function of temperature. Chapter 4 presents the obtained results and discussions for all the methods discussed in Chapter 3. The conclusions and future work are presented in Chapter 5.

2 THEORETICAL BACKGROUND

2.1 RESONATORS

A resonator is a device that oscillates at specific frequencies with high selectivity over all other frequencies. These specific frequencies are often referred to as resonant frequencies. As seen in figure 2.1 a-b, a resonator has a pair of complex poles close to the imaginary axis with a peak near its undamped resonant frequency through a sinusoidal steady-state response [24].

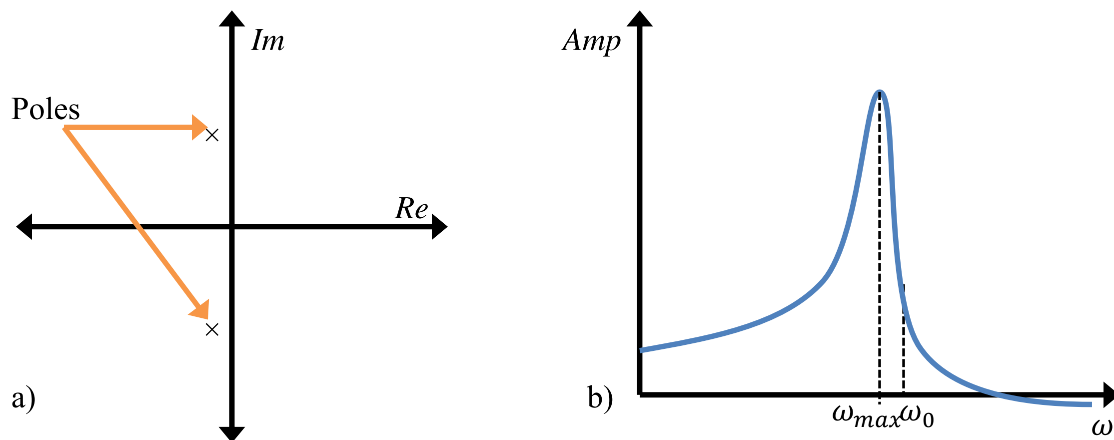

Figure 2.1 – a) Location of complex poles for a resonator, and b) resonant frequency curve.

Re and *Im* are the real and imaginary axis respectively; *Amp* and ω are the amplitude and frequency of the measured signal, and ω_0 is the undamped resonant frequency in radians per second. As it can be noticed in figure 2.1-b, the frequency that corresponds to the largest amplitude (ω_{max}) is somewhat smaller than the resonant frequency. This difference between

ω_{max} and ω_0 is due to the damping in the system --the larger the damping, the larger the difference. Other details about this figure 2.1-b are discussed in the next two sections. For each degree of freedom in a system, there is a corresponding resonant frequency that depends on the physical parameters and conditions of the system. The resonant frequencies of resonators are multiples of the lowest frequency, known as the fundamental or natural frequency. Resonators can be used as actuators (e.g. for the generation of a signal with a particular frequency), or as a sensor/detector (e.g. for detecting a signal with a specific frequency). The types of resonances relevant to this work are the electrical and mechanical resonances.

2.1.1 Electrical Resonance

Electrical resonance occurs when the imaginary parts of the impedance from the inductance and capacitance within a circuit cancel each other. When in resonance, there is no waste of electrical energy by cycling it through both elements. The inductor's magnetic field produces a current in its windings, charging the capacitor and afterwards, the capacitor discharges, producing a current that builds the inductor's magnetic field. Figure 2.2 shows an RLC circuit, which connects an inductor and a capacitor in series to produce the resonance effect for filter applications.

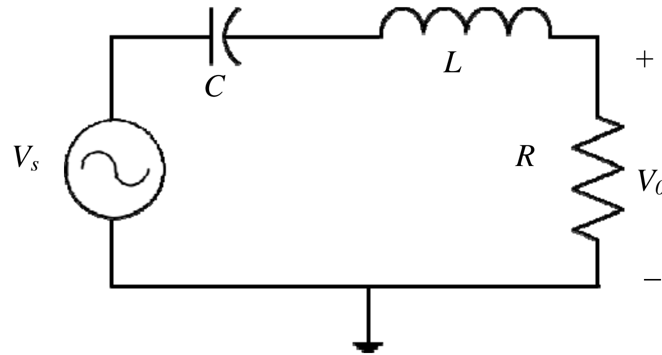

Figure 2.2 – RLC band-pass filter.

In this example, *C* is the capacitance, *L* is the inductance, and *R* is the load resistance. The resonance effect can be used to make a selective filter if the reactance of the inductor and capacitor cancel each other. In order to achieve the resonance behavior the following criteria must hold true:

$$\omega L = \frac{1}{\omega C} \rightarrow \omega_u = \frac{1}{\sqrt{LC}}. \tag{2.1}$$

Here, ω_u is the center frequency for an undamped system, for which case it is also the resonant frequency (ω_0). For a damped system, like the RCL circuit in figure 2.2, the resonant frequency is decreased by the damping factor:

$$\omega_c = \sqrt{\frac{1}{LC} - \frac{R^2}{2L^2}}\ . \tag{2.2}$$

Additionally, the resonant frequency of this filter can be tuned by changing the distance between the two capacitor plates (g) or the effective overlapping area of the capacitor (A) (see figure 2.3). A dc-bias voltage is typically used to generate an electrostatic force that will move the plates in the z direction.

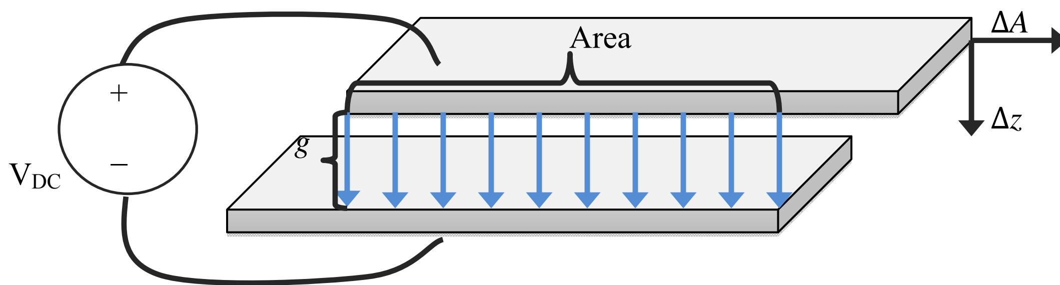

Figure 2.3 – Tunable capacitor.

2.1.2 Mechanical Resonance

Mechanical resonance, in analogy to electrical resonance, occurs when a mechanical system absorbs more energy from a driving force at a specific frequency than at any other frequency. This resonance works by transferring energy from its potential form to kinetic form repetitively in the same way energy is transferred from the capacitor to the inductor in an RCL circuit. This equivalence can be seen in figure 2.4 where the capacitance, inductance and resistance in electric circuits are the analogs to the compliance (inverse of the spring constant k), mass (m) and friction (B) of the mechanical system, respectively.

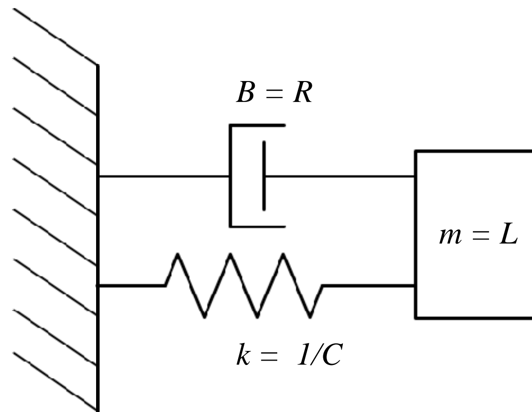

Figure 2.4 – Mechanical system elements and their respective electrical analogs.

Thus, the damped resonant frequency in a mechanical system can be estimated using the analogies in figure 2.4 which yields:

$$\omega_c = \sqrt{\frac{k}{m} - \frac{B^2}{2m^2}}. \tag{2.3}$$

It should be emphasized, however, that the analogy between electrical and mechanical resonance has limitations, and therefore it should be studied carefully before adopting an exact model. For example, as the frequency of a forced signal approaches zero in an RLC circuit, the amplitude of the current goes to zero. This is due to the inversely proportional relation that exists between the reactance of the capacitor and frequency. However, when the frequency of a forced signal approaches zero in a mechanical system (fig 2.1-b), the amplitude of the movement approaches a value proportional to the ratio between the magnitude of the applied force and the spring constant –not zero. Additionally,

mechanical systems may involve axial forces, complicating the analysis and study of the resonant frequency.

2.2 MICRO-BRIDGE MECHANICAL BEHAVIOR

A micro-bridge, shown in figure 2.5, is a beam that is supported at both of its ends. Due to these constraints, micro-bridges may develop net residual stresses during their fabrication. Such residual stress can be induced by thermal effects, such as thermal expansion. Post fabrication stresses, such as those due to external/internal axial loads or temperature gradients experienced during operation, can also affect the behavior of doubly clamped beams.

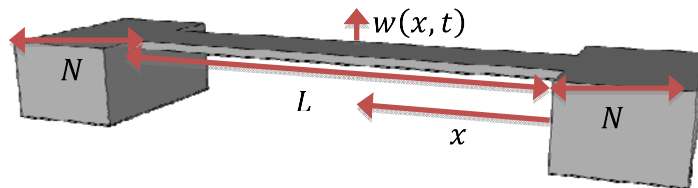

Figure 2.5 – Micro-bridge structure.

2.2.1 Transverse Vibrations

Timoshenko described the small amplitude transverse vibration by using the following partial differential equation [25]:

$$\hat{E}I\frac{\partial^4 w(x,t)}{\partial x^4} - N\frac{\partial^2 w(x,t)}{\partial x^2} = -\rho A\frac{\partial^2 w(x,t)}{\partial t^2}, \tag{2.4}$$

where $\hat{E}$ is the biaxial modulus of the material, I is the beam's moment of inertia, N is the axial tensile or compressive force, ρ is the material density, and A is the cross-sectional area of the beam. $A = WH$, where W and H are the width and height of the beam, respectively. $\hat{E} = \frac{E}{1-v^2}$, where E is the Young's modulus ($\hat{E}$ is used when $W/H > 5$); and $N = \sigma WH$, where σ is the axial stress. The boundary conditions associated to the system are:

$$\begin{gathered} w(0,t) = w(L,t) = 0\,, \\ \left.\frac{\partial w(x,t)}{\partial x}\right|_{x=0} = \left.\frac{\partial w(x,t)}{\partial x}\right|_{x=L} = 0\,, \end{gathered} \tag{2.5}$$

which means that there is no displacement or velocity at the bridge anchor points. The solution to equation (2.4) with boundary conditions from equation (2.5) is given by [25]:

$$w(x,t) = \sum_{n=1}^{\infty} X_n\left(\frac{x}{L}\right)\left(A_n cos(\omega_n t) + B_n sin(\omega_n t)\right), \tag{2.6}$$

where X_n is the shape function of the natural mode corresponding to n, $\omega_n = k_n^2\sqrt{\left(\frac{\hat{E}I}{\rho A L^4}\right)}$ is the radial frequency, and A_n, B_n and k_n are constants that depend on the boundary conditions.

2.2.2 Resonant Frequency of Unbuckled Bridges

The exact solution for the nth-mode resonant frequency of a doubly clamped beam as a function of the biaxial stress σ[i] is given by [26]:

$$f_n = \frac{\omega_n}{2\pi} = \frac{k_n^2}{2\pi}\sqrt{\frac{\hat{E}I}{\rho AL^4}}\sqrt{1+\gamma_n\frac{\sigma WHL^2}{12\hat{E}I}}, \tag{2.7}$$

where k_n and γ_n are the coefficients of the boundary conditions and the contribution of applied axial force. The first mode resonant frequency (f_{1u}) is found when $n = 1$, for which case, $k_1 = 4.73$ and $\gamma_1 = 0.2949$:

$$f_{1u} = 3.561\sqrt{\frac{\hat{E}I}{\rho AL^4} + 0.024575\frac{\sigma WH}{\rho AL^2}}. \tag{2.8}$$

Equations (2.7) and (2.8) apply to doubly clamped beam under tensile and compressive stress as long as the beam in not buckled.

2.2.3 Euler Buckling Limit

The spring constant k_{beam} for a doubly clamped bridge is given by [24]:

[i] Tensile biaxial stress is assumed positive. Compressive biaxial stress is assumed negative.

$$k_{beam} = \frac{1}{\sum_{n=1,odd}^{\infty} \sqrt{\frac{2}{L}} \frac{2}{\left(\hat{E}I{l_n}^4 + N{l_n}^2\right)}}, \tag{2.9}$$

where $l_n = \frac{2n\pi}{L}$.

The compressive stress value that makes the k_{beam} equal to zero is known as the Euler buckling limit. This limit is given by solving the denominator in the sum of equation (2.9) in terms of σ which is implicit in the variable N:

$$\sigma_{Euler} = -\frac{\pi^2}{3}\frac{\hat{E}H^2}{L^2}. \tag{2.10}$$

If the buckling limit is reached, the lateral stiffness of the beam is equal to zero and the beam deforms into its first order buckling form, which shows the cosine like deformation pictured in figure 2.6. A positive moment causes the microbridge to bend and buckle downward, whereas a negative moment causes the microbridge to bend and buckle upwards.

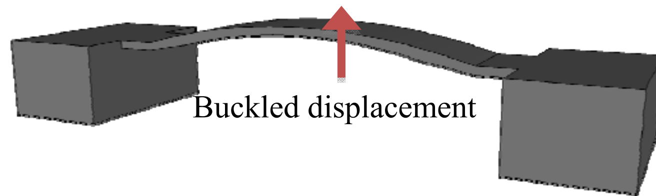

Figure 2.6 – Buckled micro-bridge.

The dynamics for a buckled micro-bridge is different than the one for the unbuckled case, and therefore the resonant frequency is not described by equation 2.7.

2.2.4 Resonant Frequency of Bukled Bridges

Nayfeh *et al*. derived the dynamics of buckled beams [27]. It was demonstrated that the first mode radial resonant frequency for a buckled doubly clamped beam is given by:

$$\omega^2 = 2\lambda^4\left(\frac{P}{\lambda^2} - 1\right), \tag{2.11}$$

where $\omega = \widehat{\omega}\sqrt{\frac{mL^4}{EI}}$, $\lambda = 2\pi$, and $P = \frac{\hat{P}L^2}{EI}$. The symbols $\widehat{\omega}$, m, and $\hat{P}$ represent the radial frequency, mass per length of the beam (ρWH), and the axial force (σWH), respectively. After some manipulation, equation (2.11) can be re-written as:

$$\widehat{\omega}^2 = 2(2\pi)^2\frac{1}{mL^2}\left(\hat{P} - (2\pi)^2\frac{\hat{E}I}{L^2}\right), \tag{2.12}$$

which is the same format presented by Southwoth *et al*. [28]. After substituting the expressions for m, I and $\hat{P}$ in equation (2.12) the radial frequency becomes:

$$\widehat{\omega}^2 = 2(2\pi)^2 \frac{1}{\rho L^2}\left(\sigma - \frac{\pi^2}{3}\frac{\hat{E}H^2}{L^2}\right). \tag{2.13}$$

The second term in equation (2.13) is the Euler buckling limit from equation (2.10). Finally, the first mode resonant frequency for the buckled micro-bridge in terms of stress/strain can be written as:

$$\frac{\widehat{\omega}}{2\pi} = f_{1b} = \sqrt{\frac{2}{\rho L^2}(\sigma - \sigma_{Euler})} = \sqrt{\frac{2\hat{E}}{\rho L^2}(\epsilon - \epsilon_{Euler})}\,. \tag{2.14}$$

Equation (2.14) applies only if:

1) The beam oscillates at small amplitudes.
2) Damping can be ignored.
3) There is no noise affecting the oscillations.
4) The geometry is uniform across the length of the beam.
5) The structure's supports can be represented by the boundary conditions.
6) The beam is composed of only one material.

Equation (2.8) can be used if the axial stress or the axial load is known while equation (2.14) requires the axial strain of the buckled beam. Figure 2.7 shows the normalized resonant frequency of a micro-bridge as a function of axial stress for the parameters and

geometry that correspond to the micro-resonator presented in this thesis using equations (2.8) and (2.14). As expected, the curves for the unbuckled and buckled micro-bridge are both zero when the stress equals the Euler stress.

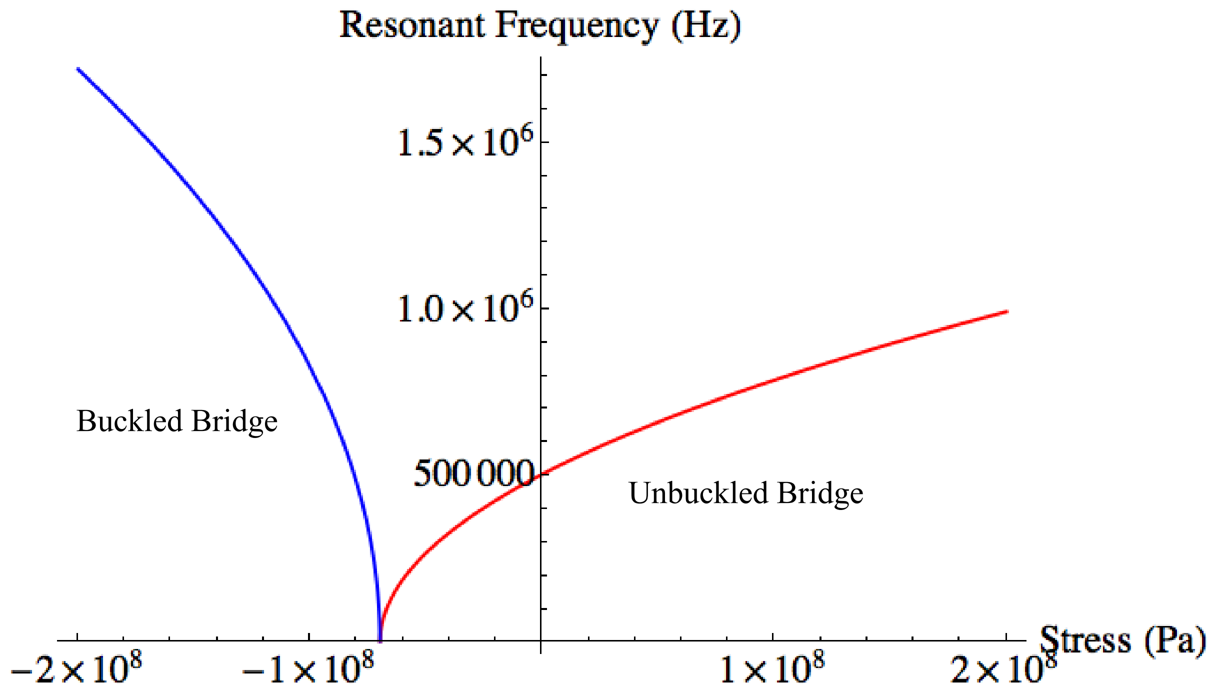

Figure 2.7 – Resonant frequency bridge as a function of axial stress for the unbuckled (red) and buckled (blue) state.

The same treatment that produced equations (2.8) and (2.14) for single-layer unbuckled and buckled micro-bridges can also be used for bimorph beams if the effective values of mass, Young's Modulus and moment of inertia are taken into account.

2.2.5 Bilayer Bridge

In this thesis, the bi-layer bridge was composed of a single material (SiO_2) bridge, coated with a thin film of VO_2. Hereinafter, the two layers composing the bi-layer bridge will be referred to as the coating and the bridge.

In order to expand the resonant frequency of unbuckled and buckled bridges to bi-layer beams, it is necessary to consider the effective values of $\hat{E}I$ and m which are given by [29]:

$$\left(\hat{E}I\right)_e = \frac{W\left[\hat{E}_c^2 H_c^4 + \hat{E}_b^2 H_b^4 + \hat{E}_c \hat{E}_b H_c H_b (4H_c^2 + 4H_b^2 - 6H_c H_b)\right]}{12\left(\hat{E}_c H_c + \hat{E}_b H_b\right)}, \qquad m_e = W(\rho_c H_c + \rho_b H_b)\,, \tag{2.15}$$

where the subscripts *c* and *b* denotes the parameters corresponding to the coating and the bridge materials, respectively. References [30-31] present theoretical and experimental results based on bilayer micro-bridges. For the unbuckled bridge, substituting equation (2.15) in (2.8) yields:

$$f_u = \sqrt{1.06\,\frac{\left[\hat{E}_c^2 H_c^4 + \hat{E}_b^2 H_b^4 + \hat{E}_c \hat{E}_b H_c H_b (4H_c^2 + 4H_b^2 - 6H_c H_b)\right]}{(\rho_c H_c + \rho_b H_b)\left(\hat{E}_c H_c + \hat{E}_b H_b\right)L^4} + \frac{0.311 \cdot \sigma H_b}{(\rho_c H_c + \rho_b H_b)L^2}}\,. \tag{2.16}$$

For the buckled bridge, substituting equation (2.15) in (2.12) gives:

$$f_b = \sqrt{\frac{2 \cdot \sigma H_b}{(\rho_c H_c + \rho_b H_b)L^2} - 6.58 \frac{\left[\hat{E}_c^2 H_c^4 + \hat{E}_b^2 H_b^4 + \hat{E}_c \hat{E}_b H_c H_b (4H_c^2 + 4H_b^2 - 6H_c H_b)\right]}{(\rho_c H_c + \rho_b H_b)\left(\hat{E}_c H_c + \hat{E}_b H_b\right)L^4}}. \quad (2.17)$$

Equations (2.16) and (2.17) describe the resonant frequency for unbuckled and buckled bridges, respectively, as a function of the biaxial stress in the beam, the material properties, and the dimensions of the bridge and its coating.

2.3 TEMPERATURE COEFFICIENT OF RESISTIVITY

The temperature dependence of resistivity for a particular material (TCR) is described by:

$$\alpha_0 = \frac{1}{\rho_0}\left[\frac{d\rho}{dT}\right], \quad (2.18)$$

where α is the TCR, ρ is the resistivity of the material as a function of temperature T, and ρ_0 is a reference resistivity at a reference temperature $T = T_0$ [32]. This coefficient is essential when fabricating electrical circuits and for many materials. For conductors, the behavior is linear through a large temperature range and therefore the TCR is simplified to:

$$\alpha_0 = \frac{1}{\rho_0}\left(\frac{\rho - \rho_0}{T - T_0}\right). \quad (2.19)$$

In equation (2.19), the TCR is the slope of the resistivity as a function of temperature multiplied by the inverse of the reference resistivity.

In the case of materials that show a non-linear TCR behavior (e.g. silicon), a different approach has to be taken in order to calculate the TCR. In reference [33], a method for calculating the numerical derivative of a finite series of samples N of the dependent with respect to the same number of samples of the independent variable is presented. This method, when applied to our case (ρ as dependent variable, and T as independent variable) yields:

$$\alpha_i\left(\frac{\%}{°\mathrm{C}}\right) = \frac{1}{2}\left[\frac{1}{\rho_{i-1}}\left(\frac{\rho_i - \rho_{i-1}}{T_i - T_{i-1}}\right) + \frac{1}{\rho_i}\left(\frac{\rho_{i+1} - \rho_i}{T_{i+1} - T_i}\right)\right] \ \forall\ i \in [1, N-1]\,. \quad (2.20)$$

Equation (2.20) calculates the TCR as the average of the slopes before and after the current value i from the finite number of data samples multiplied by the inverse of their respective reference resistivity. This method results in a discrete approximation of the derivative, which can be smooth for larger number of samples.

2.4 JUSTIFICATION

This work demonstrates the advantages of integrating VO_2 thin films with micro-mechanical resonators, particularly by allowing for a wide range of continuous tuning capability during the IMT. The IMT of the VO_2 coating can be induced thermally by conduction or optical radiation [34]. Most MEMS-based tunable resonators are excited by

electrical, electromagnetical or thermal actuation with high quality factors in micro-scale dimensions [35-39]. Frequency tuning ranges of 75% [35], 25% [36], 21% [37], 62% [38] and 17% [39] have been recently obtained and are considered the highest values that have been reached so far. However, they suffer disadvantages and limitations. The devices from references [35, 37, 38] operate at GHz with discrete switching elements which limits the values of the tunable frequencies. The GHz resonator from [36] operates at cryogenic temperatures, which is not practical for most applications. Finally, the work in [39] presents the design, fabrication and testing of a vertically shaped comb-finger. The layout of the comb-fingers is used to create electrostatic springs in silicon which tune the frequency of operation of the device. Using this method they report a frequency tune of 17%, which is the largest continuous tunable range achieved in tunable MEMS resonators to date in the kHz range. In addition to these limitations, all the best results for MEMS-based tunable resonators that have been reported (including those from [35-39]) suffer from the following common disadvantages: 1. complicated and expensive fabrication processes, 2. need of high actuation voltages, and 3. large device area. The presented technology provides continuous tuning at temperatures close to room temperature by using a simple device, which can be fabricated by following a single mask lithography process.

Although there is no reported work on VO_2-coated tunable MEMS resonators, the use of this smart material in solid-state tunable filters is a subject of study for fast response and high sensitivity applications [7, 18, 40]. However, these devices utilize the insulator-to-metal

switching capabilities of VO_2 and ignore the potentials of its continuous operation throughout the IMT.

The work reported in this thesis uses the abrupt change in VO_2 mechanical properties [9, 16, 41] (e.g. stress and Young's modulus) in order to develop a device that achieves a frequency tuning range of 23%. Furthermore, the simultaneous measurement of the resonant frequency and resistance of a VO_2-coated SiO_2 micro-bridge is studied. This structure is not only easy to fabricate, but it also occupies a very small space area which corresponds only to its dimensions. The device developed in this thesis is actuated by light radiation as proven by [41], which could be beneficial for applications that require remote tuning.

3 MATERIALS AND METHODS

3.1 SiO_2 MICRO-RESONATORS AND VO_2 DEPOSITION

In this work, a 120 nm thick VO_2 film was deposited on three SiO_2 micro-mechanical bridges (labeled 1, 2 and 3) with lengths (all in μm) of 100, 200, and 300, and widths of 45, 35 and 45, respectively. Figure 3.1 shows a top view diagram of the micro-bridges.

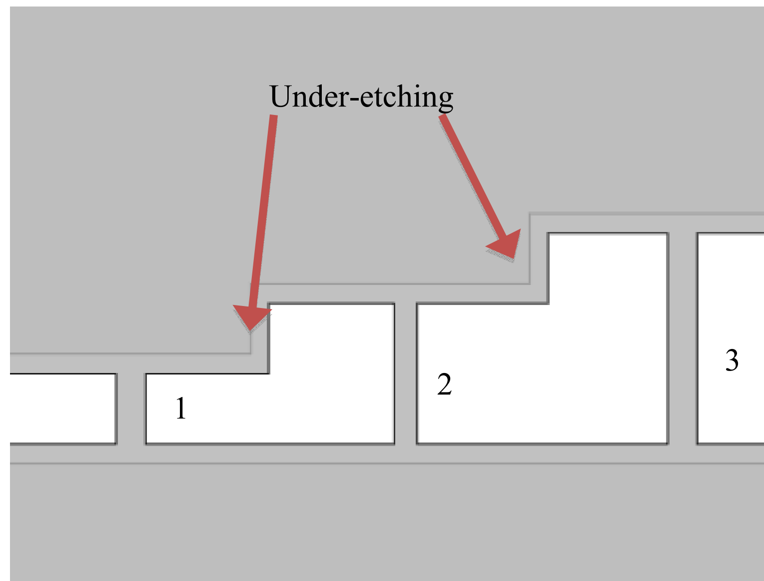

Figure 3.1 – Top view of the released micro-bridges.

Although it is not show in figure 3.1, the sample also contained a 200 μm long cantilever structure. The SiO_2 micro-resonators were fabricated by following the same standard lithography fabrication techniques reported in [10]. A standard *p*-type 4" Si wafer was used as the starting substrate and a 4.15 μm thick SiO_2 layer was deposited by using gigascale integration plasma-enhanced chemical vapor deposition. The SiO_2 micro-

mechanical bridges and cantilevers were patterned using reactive ion etching (RIE). Then, the Si wafer was diced, and the SiO_2 micro-resonators were released by using isotropic etching of the Si using xenon difluoride (XeF_2) gas. This isotropic etching also removed part of the Si underneath the anchors, creating an under-etching effect (shown in figure 3.1) that changed the effective length of the micro-bridges and cantilevers. The under-etching was measured to be 28 μm in every direction of the substrate.

The VO_2 deposition on the micro-bridges was performed by Pulsed Laser Deposition (PLD), following a similar procedure as that described in Ref. [15]. A pulsed KrF excimer laser with a fluence of 4 J/cm^2 and a frequency of 25 Hz was used to ablate a metallic vanadium target disc. The distance between the target and the sample substrate was 5 cm. The background pressure previous to deposition was in the order of 10^{-6} Torr, and from there it was raised and maintained at 20 mtorr during deposition while mass flow controllers where used to maintain 15 sccm Ar and 5 sccm O_2 gas flows. An *in situ* annealing at 370 ºC for 40 minutes in an oxidizing atmosphere with gas flows of 15 sccm Ar and 50 sccm O_2 and a total pressure of 330 mTorr was performed after deposition. The cross-sectional view of the final device is shown in figure 3.2 and a picture of bridge #2 after deposition is displayed in figure 3.3.

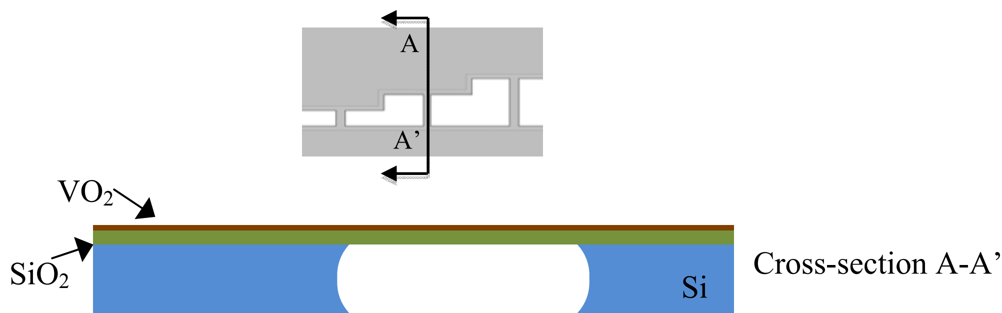

Figure 3.2 – A-A' cross-sectional view of the VO_2 coated MEMS resonator.

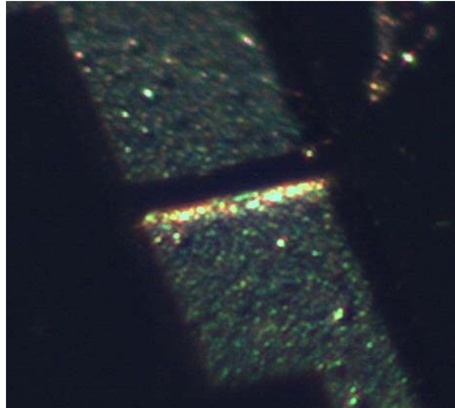

Figure 3.3 – Picture of the VO_2 coated micro-bridge.

Film composition was verified by x-ray diffraction (XRD) using a companion test piece coated simultaneously with the sample which incorporated the fabricated micro-bridge and cantilevers. XRD θ-2θ scans showed the peaks from the VO_2 film that correspond to the (011) monoclinic (M_1) reflection, meaning that the (011) plane was parallel to the substrate. Similar procedures have been used to produce VO_2 films with crystallite sizes below 100 nm [15].

3.2 MEASUREMENT SYSTEM AND PROCEDURE

The measurement setup schematic and a picture of the real setup are shown in figure 3.4 and 3.5, respectively. Measurements were conducted with the sample under vacuum in order to impede convective heat losses and reduce damping. The small vacuum chamber used for this purpose has an optical window and is pumped down to below 10 mtorr with a mechanical pump, while the pressure is monitored with a Convectron-type gauge.

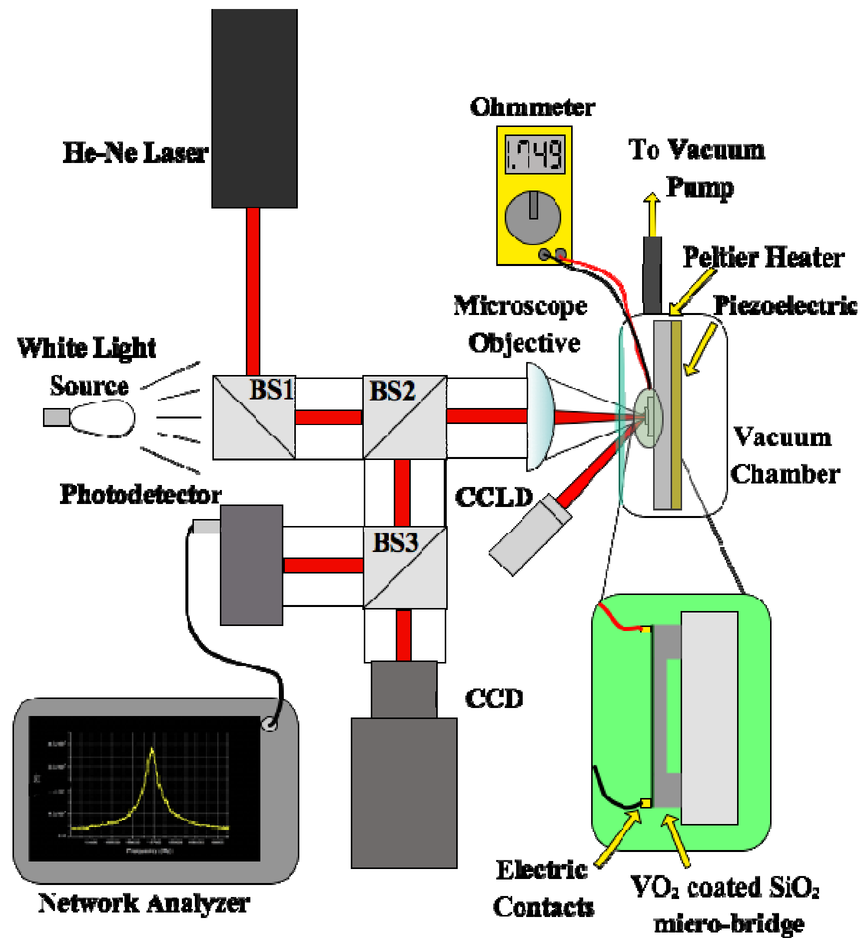

Figure 3.4 – Schematic of the simultaneous resistance and frequency measurements setup.

The sample was attached with conductive silver paste to a Peltier heater. A thermocouple was fixed to the sample in order to monitor the temperature. Gold wires attached to each of the anchor pieces were used for the resistance measurements. The resonant frequency of the bridge was measured by using a laser technique described in [9, 10, 15]. An Agilent Network Analyzer was used to actuate a piezoelectric which was glued below the Peltier heater. A frequency sweep was performed using the smallest possible signal amplitude in order to prevent non-linear behavior. A focused He-Ne 25 mW laser was aimed

at the bridge and the reflected light was guided to a photodetector. During resonance, the bridge movements produce a lateral movement in the reflected laser light spot with a frequency equal to that of the mechanical resonant frequency of the bridge. The spot's lateral movements were measured with the photodetector.

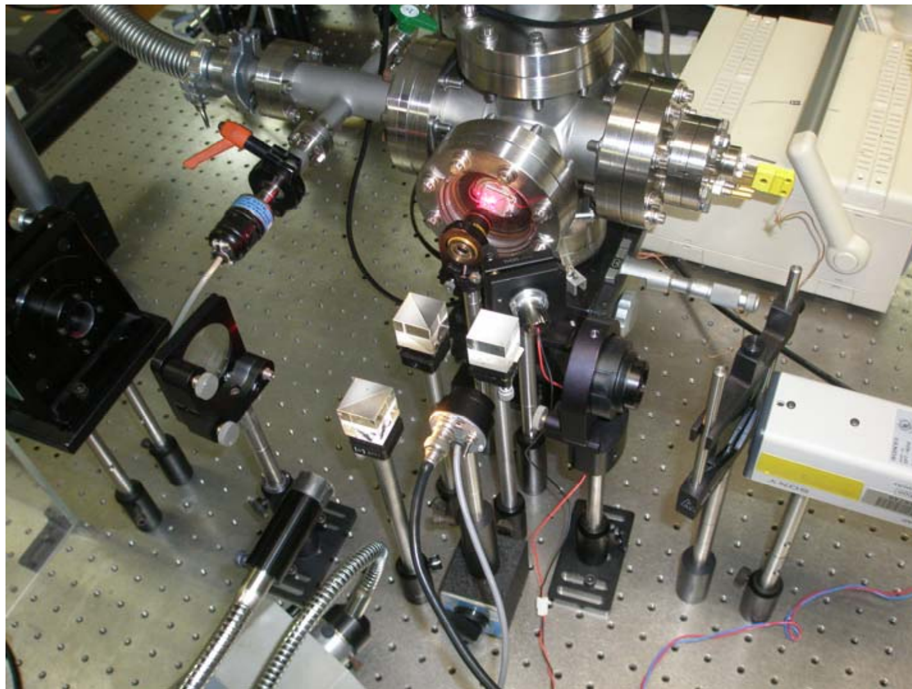

Figure 3.5 – Picture of the resonant frequency and resistance measurement setup.

A white light source was used only for assisting in positioning the 5 mW laser on the bridge and it was turned off during measurements. The light from the He-Ne laser and the white light source were combined by a beamsplitter (BS1) and focused by a microscope objective onto the VO_2-coated SiO_2 bridge. The microscope objective was used to reduce the beam spot size of the He-Ne laser, locating most of it on the coated bridge for the best

possible resonant frequency measurement. Light reflected back from the lens is separated from the incoming beams by the second beamsplitter (BS2) and directed to a third beamsplitter (BS3), which sent part of the signal to a photodetector – for determining the bridge's resonant frequency – and to a CCD camera – for visual monitoring purposes. A neutral density filter (L2) guaranteed that the CCD was not damaged by the light intensity from the current-controlled diode laser (CCDL).

The power output of the laser as a function of its input current was calibrated with an optical power meter (Thorlabs # model: PM100D). Power losses due to the glass window were measured and found to be around 8% for the entire power range, as expected. The average power density at the sample surface was estimated, after correcting for window losses and the incidence angle, from the beam diameter (~ 0.5 cm) at the distance between the CCDL and the sample. For the resistance measurements, the two electrical leads were connected externally to an ohmmeter.

This method for measuring resistance and resonant frequency was used in this work to: 1. measure the resonant frequency of the bare SiO_2 bridges shown in figure 3.1, 2. measure the resistance of the three parallel VO_2-coated SiO_2 bridges, 3. measure the resistance of the VO_2-coated SiO_2 bridge, and 4. simultaneously measure the resistance and resonant frequency of the VO_2-coated SiO_2 bridge using a conductive heating method (hereinafter referred as *conduction method*) and laser radiation method (hereinafter referred as *irradiation method*). The resistance and resonant frequency measurements of the last two experiments were performed on bridge #2 of figure 3.1.

The resonant frequency measurements of the uncoated SiO_2 bridges were used to compare the change in resonant frequency as a function of temperature with the measurements obtained from experiment 4. The data from the resistance measurements obtained in experiments 2 and 3 were used to calculate the resistivity and TCR as function of temperature of the VO_2. The temperature for the first three experiments was conductively controlled only with the Peltier heater.

The *conduction method* in experiment 4 used a Peltier heater in order to gradually increase the temperature in steps of 1ºC across the IMT while the electrical resistance and resonant frequency of the VO_2-coated SiO_2 bridge were measured simultaneously. For this actuation method, the temperature was controlled by operating the Peltier heater controller in the closed-loop configuration. The measurements were done for the complete heating-cooling cycle (30 – 100 ºC).

For the *irradiation method* experiments, the heater was controlled in "open-loop" mode to keep the temperature of the sample at ~53 ºC, which is just a few degrees before the abrupt IMT of the VO_2 film. Once the sample was at 53 ºC, the CCDL (λ=635 nm, max. power=350 mW) was used to illuminate the sample at a ~45º incidence angle. As the laser intensity was gradually increased, any temperature increase was due to irradiation from the laser beam. As in the *conduction method* experiment, the electrical resistance and resonant frequency of the VO_2-coated bridge were measured simultaneously. For this actuation method, the measurements were done for heating-cooling cycles only across the IMT region (53 – 74 ºC).

For both methods, the temperature was monitored by a thermocouple located as close as physically possible to the bridge. Due to the high resistivity of SiO_2, the measured resistance was mainly that of the VO_2 film coating only. Since the electrical resistance was measured between the two electrical contacts located at the bridge anchors, it included part of the bridge resistance as well as the series resistance between the electrical contacts and the ends of the bridge. The measured frequency corresponded to the natural resonant frequency (*i.e.* first mode) of the coated bridge.

4 RESULTS AND ANALYSIS

In this chapter, all the results obtained from the experiments explained in chapter 3 are presented. Then, a technique for calculating the resistivity of the VO_2 thin film using the basic definitions on resistivity and electric circuit analysis is explored. The TCR and temperature distribution in the resonator is also studied.

4.1 SIMULTANEOUS RESONANT FREQUENCY AND ELECTRICAL RESISTANCE

4.1.1 Conduction Method

Figure 4.1 shows the measurements of the VO_2-coated SiO_2 bridge's electrical resistance (figure 4.1-a) and resonant frequency (figure 4.1-b) as a function of temperature for the *conduction method*. The resistance undergoes a change of nearly three orders of magnitude throughout the IMT, and the shape of the curve is similar to what has been reported in the past for VO_2 films deposited on glass [2]. On the other hand, the resonant frequency curve during heating shows a small increase of 15 kHz (~3% of the room temperature value) at the "cold end" of the IMT, followed by a drop of 100 kHz (~20% of the room temperature value). For the cooling curve, the same resonant frequency curve shape is observed, but shifted down in temperature by ~5°C.

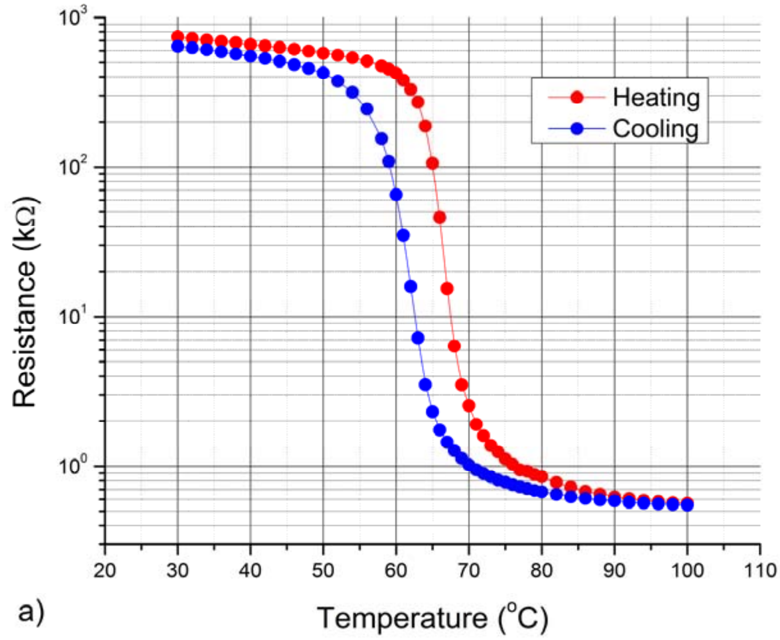

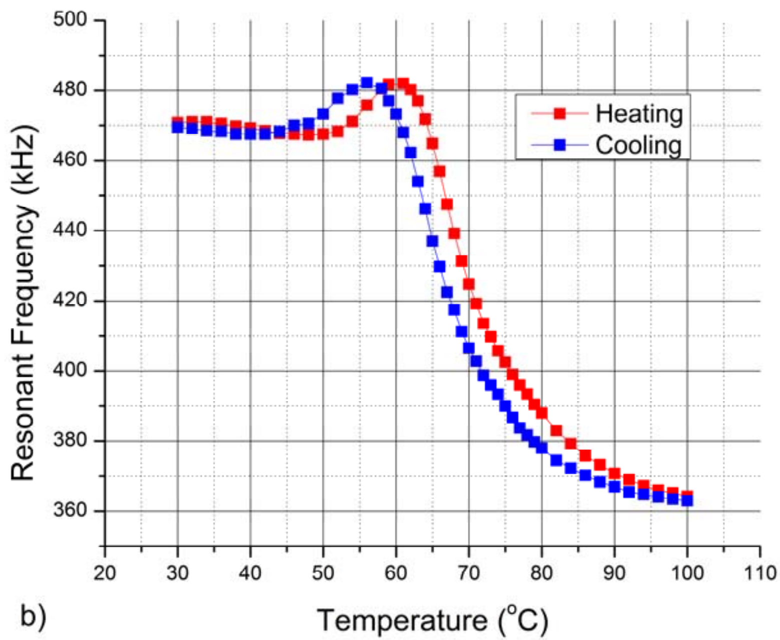

Figure 4.1 –Resistance (a) and resonant frequency (b) of the micro bridge as a function of temperature through the IMT for the *conduction method*.

4.1.2 Uncoated vs. Coated Bridge Resonant Frequency

In the search for an explanation for the rather atypical curve shape, a comparison between two 200 μm long bridges, one bare and one coated with VO_2 was done as described previously. The results are presented in figure 4.2.

Both SiO_2 micro-bridges were fabricated in the same batch and are considered to have been nominally identical before VO_2 growth. The SiO_2 film is under strong compressive stress after fabrication, due to differential thermal contraction as the sample is cooled down to room temperature from the growth temperature (~350 ℃). If this stress exceeds the buckling limit for the particular material and geometry, then the micro-bridge will buckle during the release operation. As verified with an optical microscope, the bridges used for the experiments reported here are in fact buckled after release, and remain buckled after the deposition of the VO_2 thin film is completed. The resonant frequency of the bare bridge (top line) decreases steadily as temperature increases. This is caused by differential expansion as the substrate (silicon) expands more rapidly than the bridge (SiO_2). Several authors have treated the mathematical problem of the resonant frequencies of bridges under axial stress, including the post-buckling case, as explained in Chapter 2. It was not possible in the present case to use these treatments to model the response of the bridges because of (1) the strong deviations from ideal conditions introduced by under-etching during the release operation – which alters the effective length and also invalidates the boundary conditions assumed in the theoretical models – and (2) the asymmetric residual stress introduced by the VO_2 layer. Nevertheless, the results of those models are instructive and help to explain at least some of

the features in figure 4.2. It is noted in particular that while the first mode resonant frequency (f_1) of compressed but unbuckled bridges is always lower than for the unstressed bridge (f_0), buckled bridges can have resonant frequencies $f_1 > f_0$ if compressive stress is high enough.

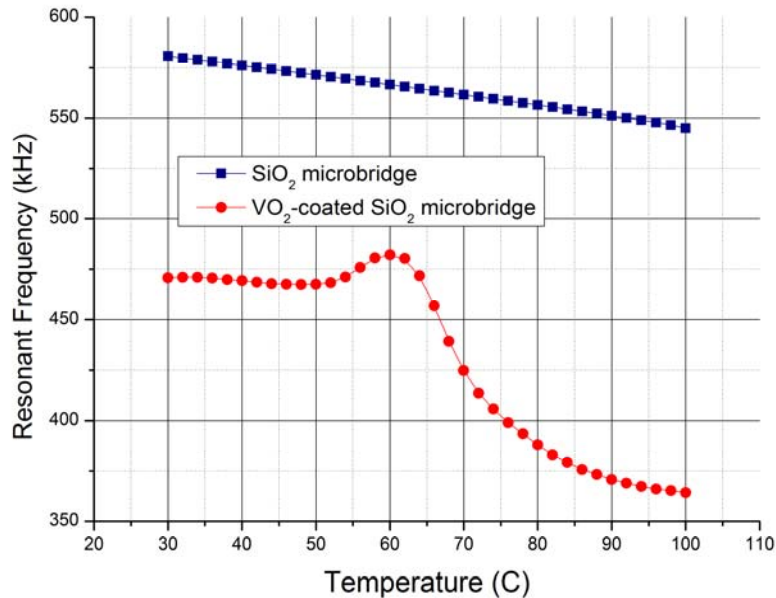

Figure 4.2 – Resonant frequency as a function of temperature for bare and VO_2-coated SiO_2 bridges.

There are striking differences between the two measured curves throughout the temperature range ($f_u (T)$ and $f_c (T)$ for the uncoated and coated micro-bridges, respectively). At room temperature, f_c is substantially lower (19% less) than f_u. As the temperature is increased up to ~50 °C f_c drops only slightly (by less than 1%) and not linearly. In comparison, over the same range f_u drops linearly by almost 2%. Afterwards, while f_u continues to drop almost linearly (the drop is actually slightly steeper by the end of the measured temperature range), f_c starts to increase as the IMT region is approached, drops quite substantially (by over 20%) through the IMT, and then continues to drop more

gradually at higher temperatures. The final f_c value at the end of the measured range has dropped by nearly 23% with respect to the RT value. For f_u the drop over the same range corresponds to just ~6% of the RT value.

For the VO_2-coated bridge there are several factors which must be considered in attempting to explain the features observed. Firstly, the bridge is now a two-layer structure or composite, and VO_2 has a larger elastic modulus, as well as larger density than the SiO_2. Secondly, there is residual stress after the film deposition and annealing process and, from previous work with VO_2 films grown on glass, it is expected that the film will be under tensile stress at room temperature [15]. Finally, all relevant material properties vary as a function of temperature, and several VO_2 properties in particular change substantially through the IMT. Only the factors relevant at room temperature are initially regarded in the following, then the effects of temperature variation are considered.

The resonant frequencies of composite stress-free bridges with uniform cross sections can be readily calculated if the moduli, densities and dimensions are known [42]. In the present case the larger effective modulus of the coating E_{film} tends to increase the resonant frequency, while its larger density ρ tends to reduce it. The elastic modulus of SiO_2 thin films can vary substantially depending on fabrication technique, but from separate experiments with cantilevers fabricated with the same process, values for the elastic modulus of ~78 GPa have been consistently obtained, and this is the value assumed in the following. For VO_2 the elastic modulus is not well known (and is anisotropic), but values from ~100 up to 200 GPa (at room temperature) have been quoted in the literature [43-46]. Assuming the lowest value

in this range for E_{film}, and bulk values for the densities of both VO_2 and SiO_2, calculation of the resonant frequencies for stress-free bare and VO_2-coated bridges using equations (2.8) and (2.16) with the geometry of the ones used in this work shows that it is higher in the latter case (by over 3%). Hence, the substantial drop from f_u to f_c measured values at room temperatures is attributed to the residual stress (tensile for the film) owing to the coating. This reduces the effective (compressive) axial stress on the buckled bridge, and thus causes a reduction of the resonant frequency. This effect is large enough to overcome the increase in f_c with respect to f_u which would be expected to occur otherwise. As can be deduced from equation 2.17, the relative importance of the two opposing effects will depend on the thickness ratio of the two materials: the effect of stress is dominant for the low thickness ratio in the present case ($t_{film}/t_{glass} = 0.027$).

4.1.3 Resistance and Resonant Frequency Curves

As the temperature is increased from room temperature there are several competing factors which can affect the frequency, but the main ones, at least up to ~50 °C are related to thermal expansion. As for the bare micro-bridge, the span between the anchors expands more rapidly than the SiO_2 bridge, but in addition the stress caused by the VO_2 film begins to change, because the film material expands more rapidly that the SiO_2. Since VO_2 is monoclinic in this temperature range, its expansion coefficient is anisotropic (and therefore different for different crystallographic planes) but its average value is 5.7 x 10^{-6} K^{-1} [46], which is almost an order of magnitude higher than the value for bulk SiO_2, and about twice

the value for silicon at room temperature. The effect of the relative expansion of the span still dominates and as a result the resonant frequency is reduced with temperature, but the reduction is partially compensated by the stress change caused by the expansion of the VO_2 film. After ~50 ºC the IMT region is approached. The width of this transition region depends on film growth conditions, but as may be seen from the simultaneously measured curve for the VO_2 resistance (figure 4.1-a), its value begins to drop more steeply by ~55 ℃, which means that for this particular sample the IMT region is rather broad. After this temperature value the measured resonance increases rather rapidly and peaks near 60 ℃, then beginning a steep descent through the rest of the IMT region. While it seems reasonable that the observed peak is caused by changes in the interplay of stresses caused by thermal expansions, the particular mechanism causing the resonant frequency to increase substantially in the range from 55 º to 60 ℃ it is not presently clear. As the IMT progresses, however, the transformation of VO_2 micro-crystals from monoclinic to tetragonal phase is accompanied by a reduction in the area corresponding to the $(011)_{monoclinic}$ crystallographic planes parallel to the substrate, as these transform into $(110)_{tetragonal}$ planes. This effect has been discussed elsewhere for VO_2 films deposited on silicon micro-cantilevers [16], and was also observed in the SiO_2 cantilevers located next to the bridges (*vide infra*). This film contraction causes a substantial change in tensile film stress through the IMT. It is noted that this effect, caused by the phase transformation itself, is not due to thermal expansion of the VO_2, and in fact has the opposite sign. Hence the increased stress on the bridge has an effect which is now in the same sense as that caused by thermal expansion of the bridge span, but much more rapid: as a

result the resonant frequency drops markedly. After the IMT region is passed, which in this sample – again from the simultaneous resistance measurements – can be considered to happen near 80 ℃, the resonant frequency continues to drop more gradually, with no sudden change in the rate of decay with respect to temperature, and by the end of the measured range this rate is nearly the same as for the uncoated bridge. Because the expansion coefficient of VO_2 in its tetrahedral phase is much higher than in its monoclinic phase [46], it could be expected that the resonant frequency would start to increase slightly or at least level off shortly after the IMT. However, this is not what is observed in this last portion of the range, and it appears that other factors dominate. Since the property coefficients for both Si and SiO_2 are expected to have only minor variations over this extent of only ~ 10 to 15 degrees, it is suggested that the still relatively rapid change of VO_2 properties – such as a reduction in its effective elastic modulus for the tetrahedral phase – may be responsible for the response observed.

4.1.4 VO_2-coated SiO_2 cantilever

In [16], the authors studied the bending of VO_2-coated Si cantilevers across the IMT. It was observed that, in the heating cycle, the bending of the bimorph cantilever was initially slightly concave toward the cantilever side (VO_2 film coating in compression), followed by a significant bending in the opposite direction (VO_2 film coating in tension). The experiment was repeated for a 200 μm long, VO_2-coated SiO_2 cantilever from the same chip of the VO_2-coated bridges, and observed this same behavior during the heating cycle across the IMT. For

the cooling cycle, a very similar bimorph cantilever bending behavior with opposite sequence was observed, as expected. This indicated that the VO_2 film experiences a reversible small expansion-large contraction sequence during the heating cycle across the IMT (contraction-expansion for the cooling cycle), causing a reversible sign-changing extrinsic stress in the bimorph cantilever across the IMT. Figure 4.3 shows the resonant frequency shift of the VO_2-coated cantilever.

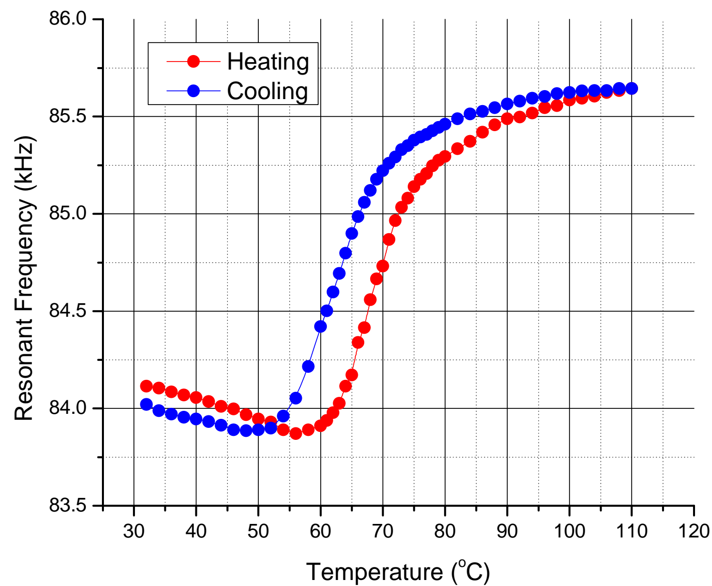

Figure 4.3 – Resonant frequency as a function of temperature for a 200 μm long VO_2-coated SiO_2 micro cantilever (*for conduction method*).

It can be noticed that the resonant frequency was practically constantly increasing across the IMT with the typical VO_2 hysteresis curve shape, in accordance with previous observations [9,15]. Unlike the cantilever beam, where most of the extrinsic stress is relieved due to the free end, a bridge structure stores this reversible extrinsic stress developed across

the IMT. This is most likely the reason why the behavior of the resonant frequency for the coated micro-bridges is much more pronounced than for the coated cantilevers.

4.1.5 Irradiation Method

Figure 4.4-a shows the power output of the laser as a function of its input current calibrated with an optical power meter (Thorlabs model PM100D). Power losses due to the glass window were measured and found to be around 8% for practically the entire power range. The optical power density (OPD) at the sample surface was estimated, after correcting for window losses and the incidence angle, from the beam diameter (~0.5 cm) at the sample distance with the following equation:

$$OPD = \frac{Transmitted\ Power}{Area} = \frac{0.92\cos\left(\frac{\pi}{4}\right) * OP}{\pi 0.25^2}, \tag{4.1}$$

where OP is the optical power (in mW) measured by the optical power meter, the term 0.92 is the transmittance through the window (the losses due to the window are 8%), $\cos\left(\frac{\pi}{4}\right)$ is the term which takes into account the incidence angle of the laser, and the denominator is the area of the spot assuming a circle with a radius of 0.25 cm. The units for OPD are mW/cm^2. A linear relationship between OPD and temperature can be found by using equation (4.1) and the measured temperature at each OPD value. Figures 4.4-a and -b show the linear relationship between the laser input current and optical power; and optical power density and temperature, respectively. This information will be used to compare the two thermal actuation methods used.

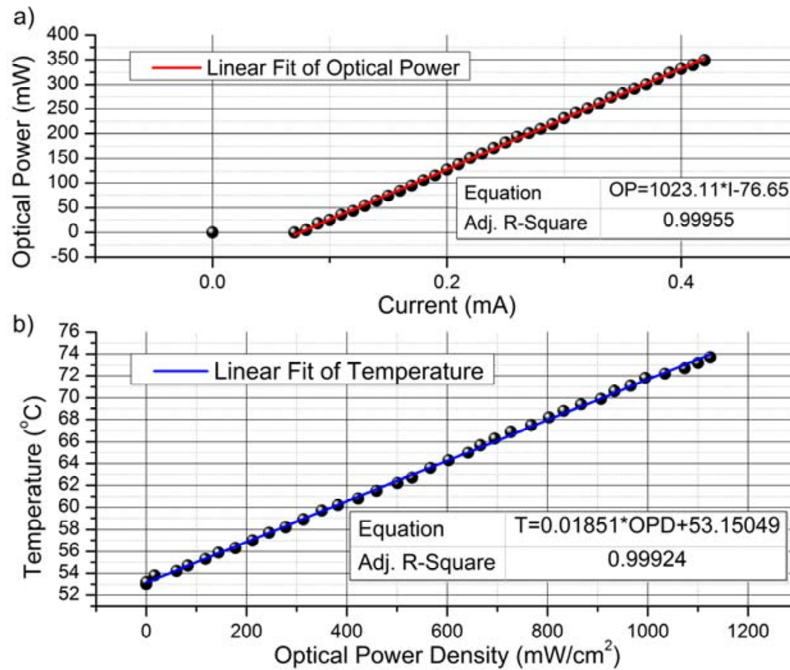

Figure 4.4 – Optical power calibration as a function of the current supplied to the diode (a) and sample temperature measured with the thermocouple as a function of optical power density on the sample (b).

As explained in Chapter 3, the measurements for the *irradiation method* were done only for the IMT region. Figures 4.6-a and -b show the results obtained from this method for the VO_2-coated SiO_2 bridge's electrical resistance (which actually is mostly the VO_2 film resistance) and resonant frequency, respectively, as a function of temperature. The insets in figure 4.6 show the results as a function of power density. A very similar behavior to the one observed for the *conduction method* across the IMT can be observed. This demonstrates that the VO_2-coated SiO_2 resonators described can be remotely tuned by inducing heating with laser light, and show the typical and expected behavior that would show if conduction heating was used, confirming the potential use of the developed technology for reliable low-power wireless tunable resonators.

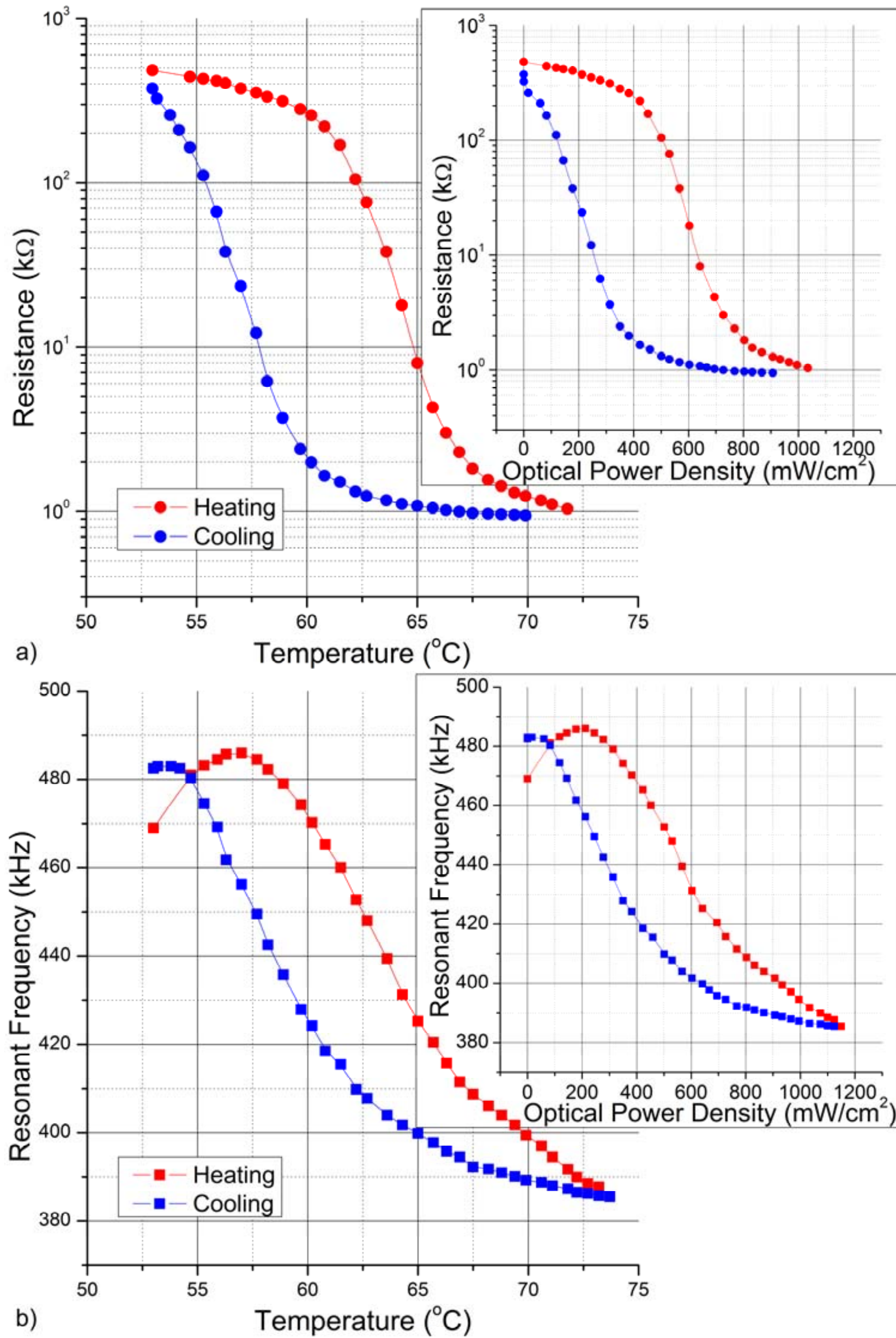

Figure 4.5 – Resistance (a) and resonant frequency (b) of the micro bridges as a function of temperature thru the IMT for the *irradiation method*.

4.1.6 Comparison Between Actuation Methods

Figure 4.6-a and -b shows the comparison between the two actuation methods. It can be noticed that although both methods show practically the same change in resistance across the IMT, the heating-cooling curves that correspond to the conduction heating method are shifted to the right with respect to the optical method curves. This shift is most likely due to the temperature gradient between the thermocouple and the coated bridge. For the *irradiation method*, the bridge is illuminated from the top (coating side). In this scenario, optical power is converted to thermal energy at the bridge coating. The energy is then transferred to the bridge and then to the chip substrate, where the thermocouple was placed. For the *conduction method*, heat was transferred from the Peltier to the sample holder, then to the chip substrate, then to the bridge, and finally to the VO_2 coating. Therefore, for the *irradiation method*, the VO_2 film was at a slightly higher temperature than the thermocouple; whereas for the heater method the opposite was true. If it was physically possible to measure the exact temperature at the coated bridge, both pairs of curves should meet somewhere in between the range of temperature that separates them. In addition, it is noted that the shapes of the two curves are not identical. This is due in part to the fact that the maximum available laser power was not enough to heat the sample past the transition region entirely. By the end of the cooling portion of the laser-heated cycle it is no longer true that the temperature of the bridge region is expected to be higher than that of the anchor region. In fact, the end of the cooling branch of this curve actually meets the corresponding curve for the Peltier-heated cycle.

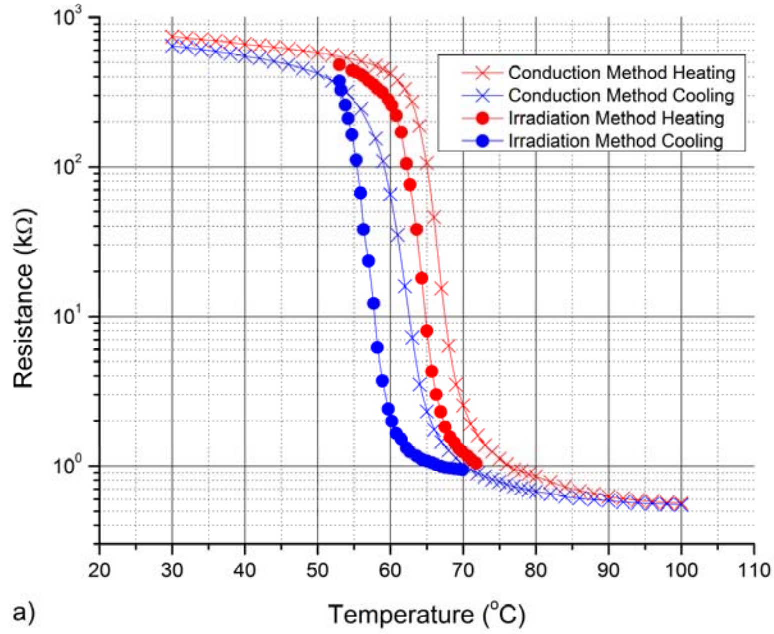

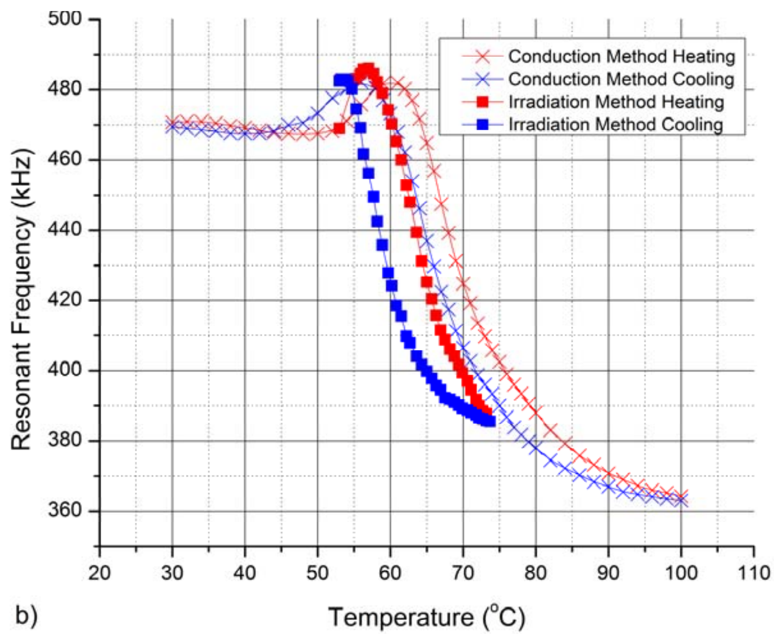

Figure 4.6 – Comparison between the two heating methods, conduction and irradiation for the resistance (a) and resonant frequency (b) change as a function of temperature.

In order to justify the assumptions regarding the difference in behavior between the two actuation methods, an FEM heat transfer analysis of the structure was done. Figure 4.7 shows the geometry used in the simulation where the complete system was considered, including the glass and silicon substrate. The heating due to laser illumination and conduction from the Peltier heater were simulated using two bounded inflow heat fluxes; marked as "*Laser Spot*" and "*Glass Substrate*" in Figure 4.7, respectively. The "*Thermocouple*" boundary represents the area where the thermocouple was placed for temperature monitoring.

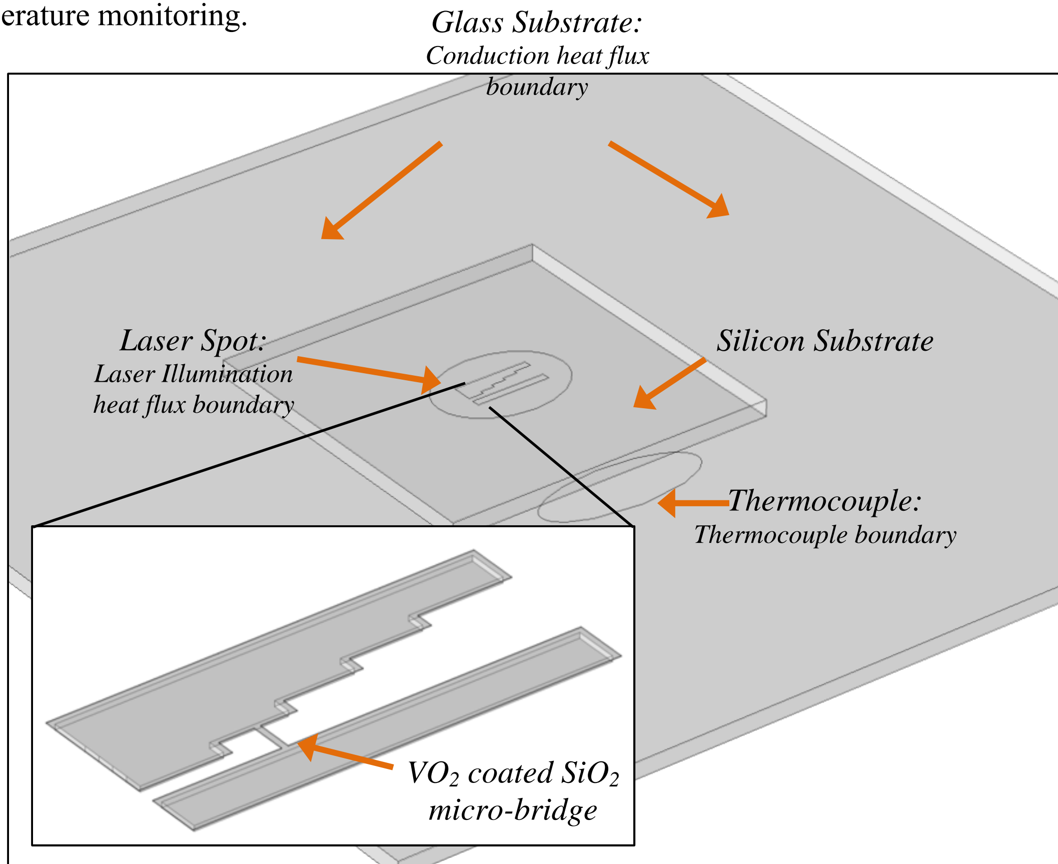

Figure 4.7 – Geometry of the micro-resonator simulated in COMSOL. The inset shows the VO_2 coated SiO_2 micro-bridge more clearly. Under-etching effects were considered.

Since all measurements were done in vacuum, the entire geometry was drawn inside a domain with air at low pressure (10^{-3} Torr). The thermal parameters for each of the materials used in the simulation are listed in figure 4.8. Bulk values for heat capacity (C_p), thermal conductivity (k) and density (ρ) for silicon and SiO_2 were used. For VO_2, the thermal properties were taken from literature [47,48].

Materials	**Density** $\left(\frac{kg}{m^3}\right)$	**Thermal Conductivity** $\left(\frac{W}{m\,K}\right)$	**Heat Capacity** $\left(\frac{J}{kg\,K}\right)$
Silicon	2,329	130	712
Silicon Dioxide	2,200	1.4	730
Vanadium Dioxide	4,670	5	678

Figure 4.8 – Thermal properties of the materials simulated in COMSOL.

The same experimental setup described for the *conduction* and *irradiation methods* was recreated in this simulation in order to study the difference in temperature from the thermocouple boundary and the bridge, and the temperature distribution in the bridge. For the simulated *conduction method*, the *Glass Substrate* boundary was used to increment the temperature of the *Thermocouple* boundary. For the simulated *irradiation method*, the *Glass Substrate* boundary was fixed so that the temperature at the *Thermocouple* boundary measured 53 °C. Then, the heat flux in the *Laser Spot* boundary was used to increase the temperature further.

The average temperature of the bridge was compared to the average temperature in the *Thermocouple* boundary, shown in figure 4.9, for both actuation methods. It can be seen that both simulated methods yield different results. For the simulated *conduction method*, the

bridge is at the same temperature than the thermocouple for every inflow heat flux value, whereas for the simulated *irradiation method* the bridge has a higher temperature slope compared to the thermocouple's temperature as a function of heat flux. This helps explaining the transition temperature differences observed in figure 4.6.

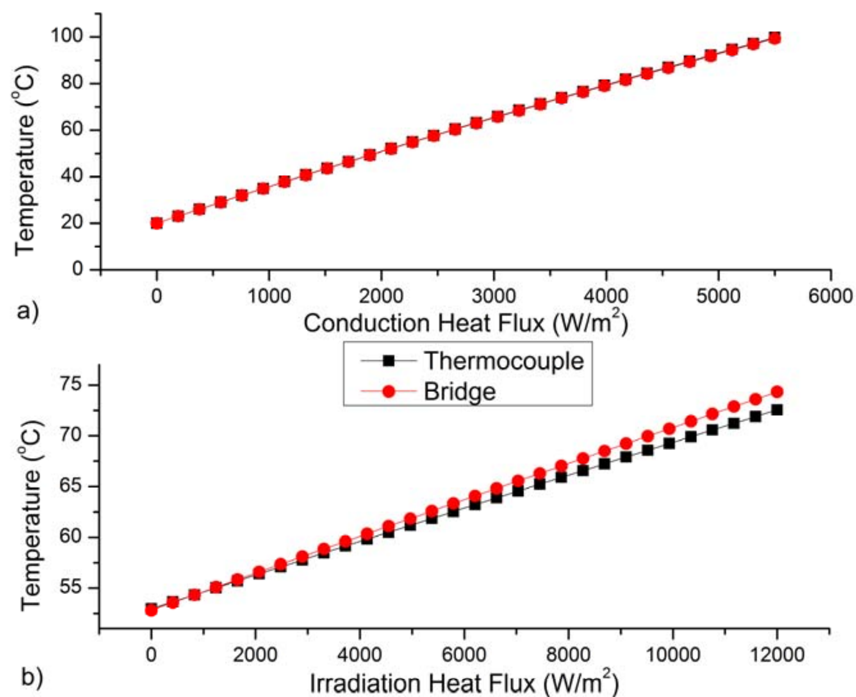

Figure 4.9 – Average temperature at the bridge and thermocouple boundary as a function of inflow heat flux for the simulated *conduction* (a) and *irradiation* (b) *methods*.

The temperature distribution in the bridge for both simulated actuation methods is presented in figure 4.10. For the simulated *conduction method* the temperature distribution is uniform throughout the bridge length, whereas for the simulated *irradiation method,* the temperature across the bridge varies significantly having a peak temperature in the center of

the bridge. This temperature distribution also explains the differences between data obtained with both actuation methods.

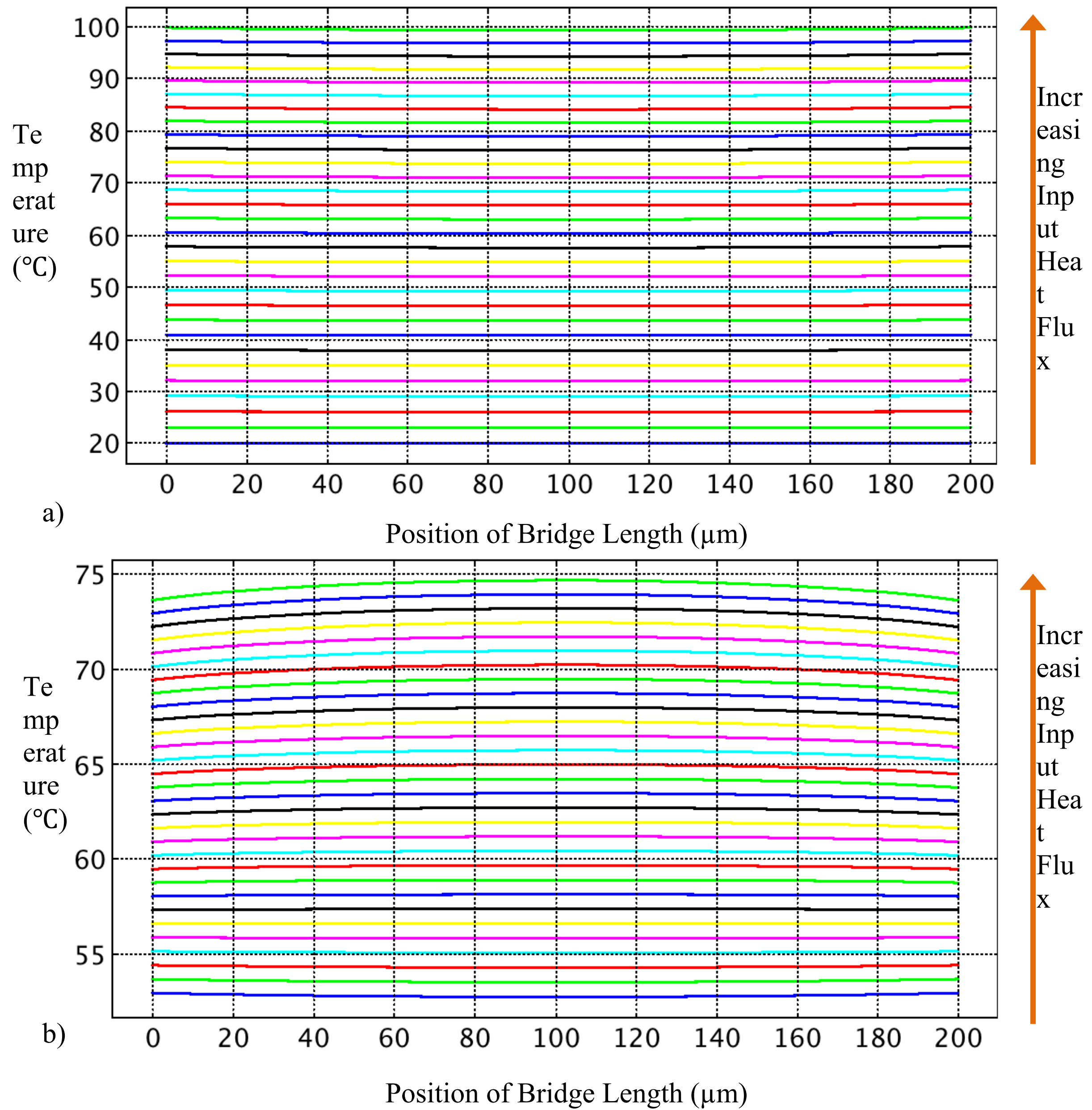

Figure 4.10 – Temperature as a function of bridge length for the simulated *conduction* (a) and *irradiation* (b) *methods*.

4.2 RESISTIVITY AND TCR

The sample discussed in the previous section consisted initially of three bridges with different dimensions connected in parallel through common anchors at both ends, as shown in figures 3.1 and 4.11.

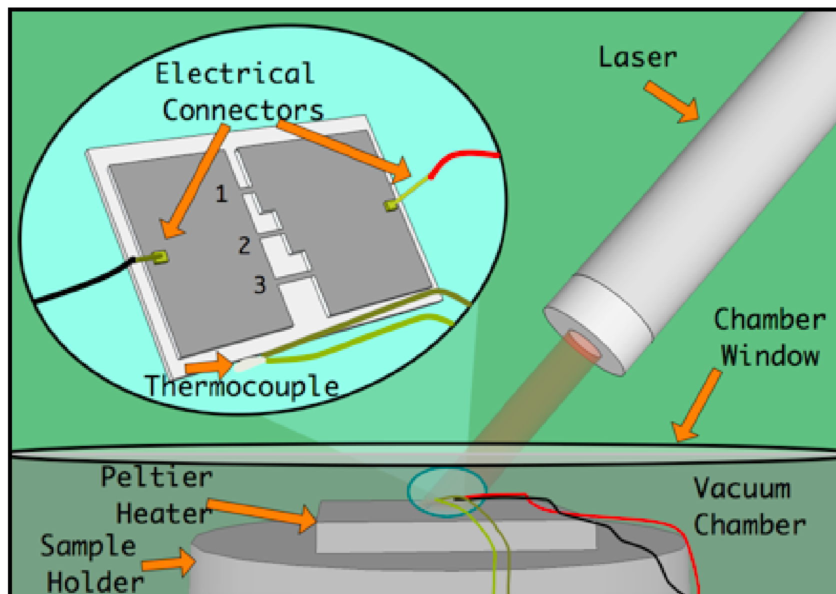

Figure 4.11 – Setup for resistivity calculation using optical radiation and conductive heating with the three parallel bridges and one bridge experiments. The bridges are numbered from 1to 3.

Since the distance between the electric connectors and the three bridges is larger than - or at least comparable to - the distance between the three bridges, the electrical resistance of the parallel bridge configuration can be expressed as:

$$R_{3t} = R_{s1} + \frac{\rho L_1 L_2 L_3}{A_1 \left(L_1 L_2 + L_2 L_3 + \frac{L_1 L_3 A_2}{A_1} \right)} + R_{s2} \, , \tag{4.2}$$

where R_{3t} is the resistance of the structure with the three bridges connected in parallel; R_{s1} and R_{s2} are the series resistances from the electrical connection at the bridges' supports to the suspended bridge (see figure 4.11); ρ is the resistivity of the VO_2 thin film; L_1, L_2, and L_3 are the lengths of the bridges, respectively; A_1 is the cross-sectional area of bridges 1 and 3; and A_2 is the cross-sectional area of bridge 2. Bridges 1 and 3 were wider than 2, which is the reason for the different form of the third term in the denominator in equation (4.2). R_{3t} was measured for heating-cooling cycles across the IMT using the two methods described before. Two bridges were then intentionally broken off using a manipulator probe, leaving only the 200 µm long 35 µm wide VO_2-coated bridge. For this one-bridge configuration, neglecting the change in resistance of the bridge support sections, the sample's resistance R_{1t} can be approximated as:

$$R_{1t} = R_{s1} + \rho \frac{L_2}{A_2} + R_{s2} \, , \tag{4.3}$$

Since the resistance corresponding to the bridges themselves can be calculated analytically due to their simple geometry, the resistance corresponding to the anchor areas (R_{s1} + R_{s2}) can be estimated by subtraction of the resistance of the three parallel bridges (three-bridge case)

or of bridge #2 (one-bridge case). The values obtained for the total anchor area resistance in each of the two configurations was found to differ by ~ 5%.

Hence, with this approximation, equations (4.2) and (4.3) can be combined to eliminate the common $R_{s1} + R_{s2}$ term, yielding the following expression for the VO_2 film's resistivity:

$$\rho = \frac{(R_{1t} - R_{3t})A_2\left(L_1L_2 + L_2L_3 + \frac{L_1L_3A_2}{A_1}\right)}{L_2^2(L_1 + L_3)}. \quad (4.4)$$

Naturally, the foregoing also assumes that a single resistivity value is applicable through the structure, which is clearly not true due to the temperature gradient expected between the bridges and the anchor zones. After measuring R_{1t} and using the previous results for R_{3t} (equation 4.2), equation (4.4) was used to calculate the film's resistivity as a function of optical power density (figure 4.12-a) or sample temperature (Fig. 4.12-b) through the IMT.

Figure 4.12-a presents the results obtained during the heating-cooling cycle of the sample using the *irradiation method*. The resistivity undergoes a change of nearly three orders of magnitude throughout the IMT and its value is close to that found in literature [1, 2]. Figure 4.12-b shows the same cycle (graph with circles) in terms of the temperature measured with the thermocouple, and a second cycle for the *conduction method* (graph with crosses). Note that the latter starts from room temperature, but the former starts from 53ºC, as explained before.

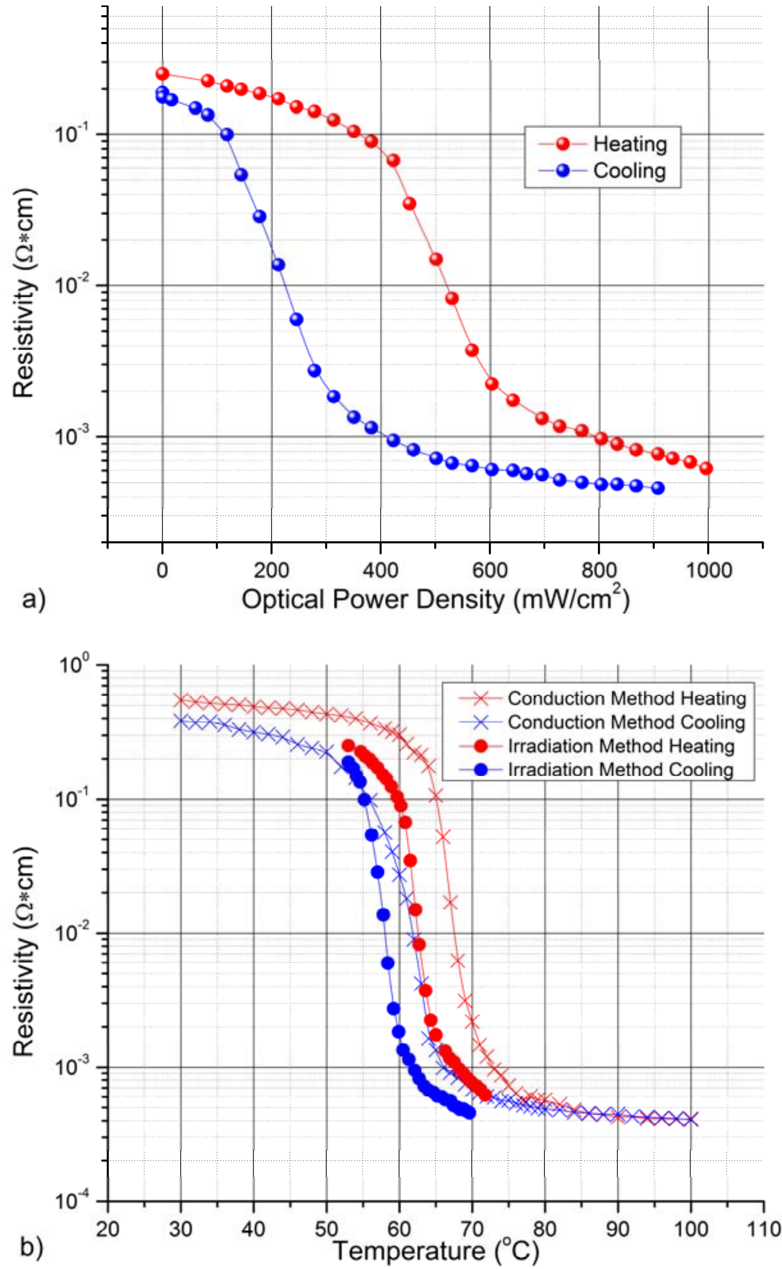

Figure 4.12 – Calculated resistivity as a function of delivered optical power (a) and temperature (b) for heating-cooling cycles for the conduction (2 curves with "x" symbol), and irradiation methods (2 curves with "●" symbol).

The resistivity values obtained can be used to calculate the TCR of the VO_2-coating on the SiO_2 bridges as a function of temperature or irradiance on the sample. The TCR is defined by equation (2.18), which can be transformed into the discrete expression in equation (2.20). Figure 4.13 shows the TCR as a function of temperature and of incident irradiance (inset). Due to the rapid change in resistivity of the VO_2 through the IMT, the TCR shows sharp minima at the transition values. The minima for heating and cooling are of course shifted in the same way as the resistivity curves. As may be seen more clearly from the TCR curves, this shift corresponds to nearly 300 mW/cm^2, which is approximately the largest width of the hysteresis curve in figure 4.12-a. The width of the region with deeper TCR values for both branches has a similar or slightly higher value. Peak TCR values obtained were -85 %/℃ during the heating process and -80.8 %/℃ during cooling. The values characterizing the IMT in VO_2 depend strongly on film growth conditions and substrate material, and therefore it is possible to obtain desired characteristics in a rather ample range. It is also feasible to engineer the response of the material – including shifting the transition temperature - by doping with suitable ions [49, 50].

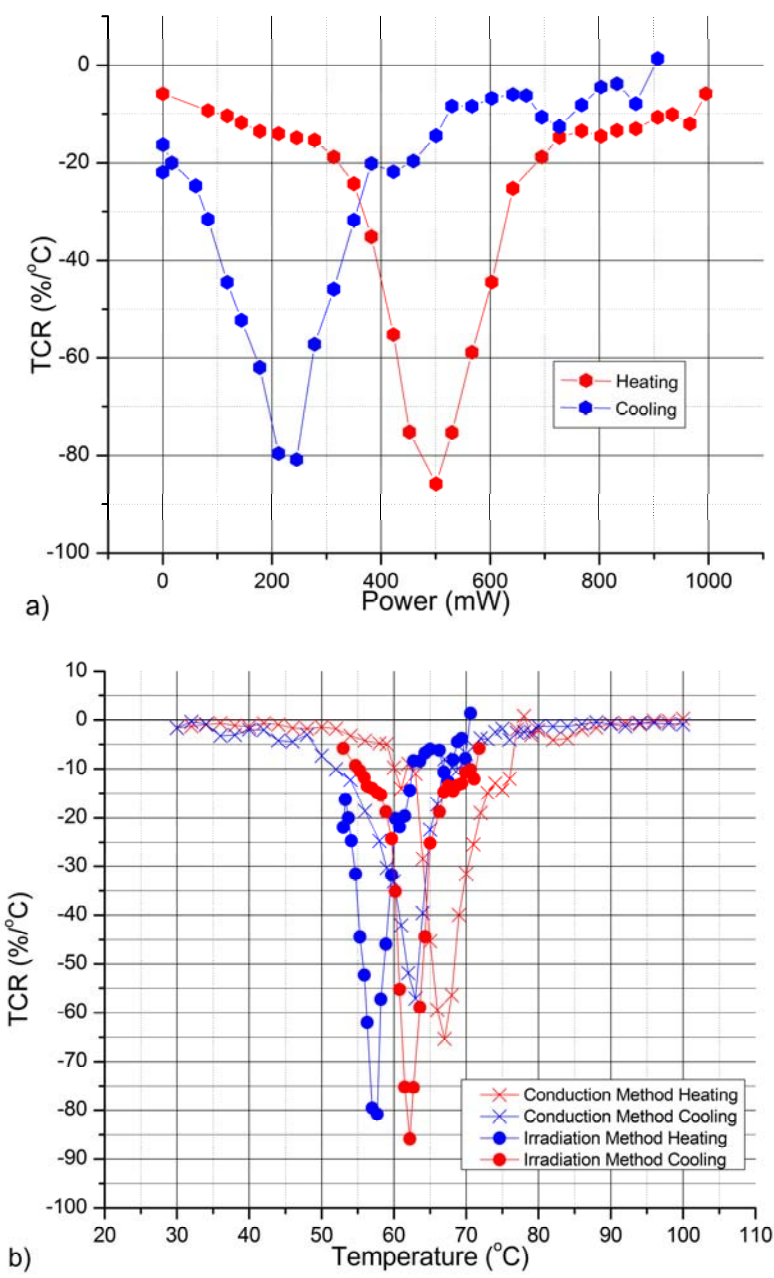

Figure 4.13 – Calculated TCR as a function of delivered optical power (a) and temperature (b) for heating-cooling cycles for the conduction (2 curves with "x" symbol), and *irradiation methods* (2 curves with "●" symbol).

5 CONCLUSIONS AND FUTURE WORK

5.1 CONCLUSION

This work presented the development of a VO_2-coated SiO_2 micro-bridge resonator with a 23% tunability range, which makes it the MEMS-based tunable resonator with the highest tunability in the kHz range. The resonant frequency and resistance of the microstructure were measured simultaneously as a function of temperature through the VO_2's IMT during heating and cooling cycles. In order to increase/decrease the device's temperature, two actuation methods were used: the *conduction method*, where a Peltier was used to heat the device through conduction, and *the irradiation method*, where a 635 nm wavelength red laser heated the device through light radiation. The differences between the actuation methods were discussed and explained using FEM simulations. The resistivity of the VO_2 film as a function of temperature was calculated from experimental data using each heating method. In both cases the temperature coefficient of resistance was obtained as a function of irradiance or sample temperature through the heating-cooling cycles.

The results showed a three orders of magnitude drop in resistance and a 23% frequency tuning capability for VO_2-coated micro-bridges caused by the large stresses developed across the IMT as the film compresses. Although the device structure show a strong deviation from ideal conditions due to under-etching effects from the fabrication process, and buckling, which results in a non-uniform stress distribution throughout the

bridge, the device's behavior was qualitatively explained with theory available in literature. Since these structures were not optimized for maximal stress change, which can be affected, for example, by film thickness or growth temperature, it is likely that even higher tuning ranges can be obtained with micro-bridges.

5.2 FUTURE WORK

In order for this high tuning capability to be useful, the precise control of the VO_2 hysteresis behavior is required for high performance tunable resonators. Hysteresis and nonlinear modeling and control are two major topics that play an important role in MEMS devices.

Future work will address the use of robust control algorithms that compensate for the hysteretic behavior in VO_2. Through the use of the Preisach operator and parameter identification techniques a dynamic model for the micro-resonator's hysteretic behavior can be found from experimental data. Another important improvement that can be performed to this device is to fabricate the micro-bridge with precision etch stops. This would eliminate the under-etching which prevents the use of theoretical models describing the resonant frequency behavior as a function of stress. Since this resonant frequency is strongly dependent on the buckled micro-bridge's initial deflection, this deflection can be measured as a function of temperature and used to calculate the theoretical resonant frequencies through the tuning range.

APPENDIX A THE PREISACH MODEL

A.1 The Preisach Operator

The Presiach Operator Γ is a hysteresis phenomenological model describe by [51]:

$$\Gamma[u, \Psi_0](t) = \iint_{P_0} \mu(\beta, \alpha)\, \hat{\gamma}_{(\beta,\alpha)}[u, \Psi_0(\beta, \alpha)](t)\, d\beta d\alpha\,, \tag{A.1}$$

where u is the hysteretic input, μ is the weighting function of the operator, β and α are threshold parameters $(\beta \leq \alpha)$ for the hysteretic element $\hat{\gamma}_{(\beta,\alpha)}$, Ψ_0 is the initial configuration of the Preisach operator and P_0 is the Borel measure. Figure A.1 shows a single Preisach hysteron which is the elementary and most basic operator.

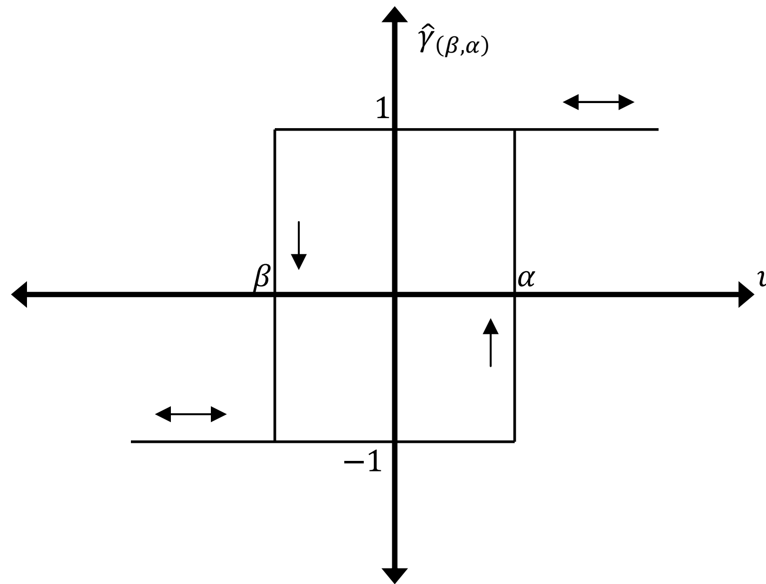

Figure A.1 – The Preisach hysteron.

The discretized Preisach operator, shown in figure A.2, is the superposition of these self-adjoint operators, sown in figure A.1, which have their own local memory.

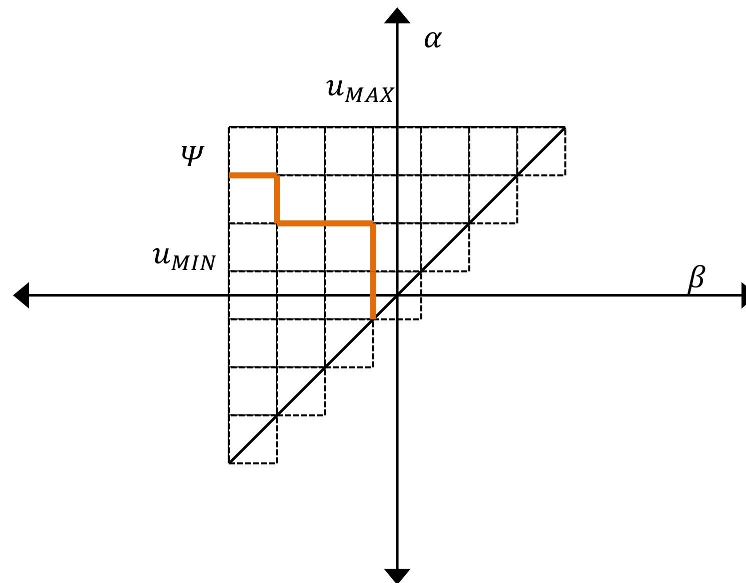

Figure A.2 – The discretized Preisach operator.

Each one of the squares in the discrete operator in figure A.2 is a hysteron with its own (β, α) thresholds. The system input u has a range of $[u_{MAX}, u_{MIN}]$ and Ψ is the hysteretic memory or trajectory. The operating principle of the Preisach operator is summarized in figure A.3 (a)-(d) where the operator is subjected to an input sequence $[u_0, u_1, u_2, u_3]$ where $u_1 > u_3 > u_2 > u_0$. In figure A.3-(a) the initial input $u_0 = u_{MIN}$ and thus, the trajectory is set to $\Psi = \Psi_0$. As the input is increased to u_1, the trajectory moves up with the input along the $\alpha = \beta$ diagonal forming a horizontal line. Then, the input is decreased to u_2 and the trajectory moves to the left forming vertical line with a corner. It is this behavior that stores

memory in the Preisach operator. Since the last value $u_3 > u_2$ a horizontal line again appears and the trajectory moves up ones more forming another corner.

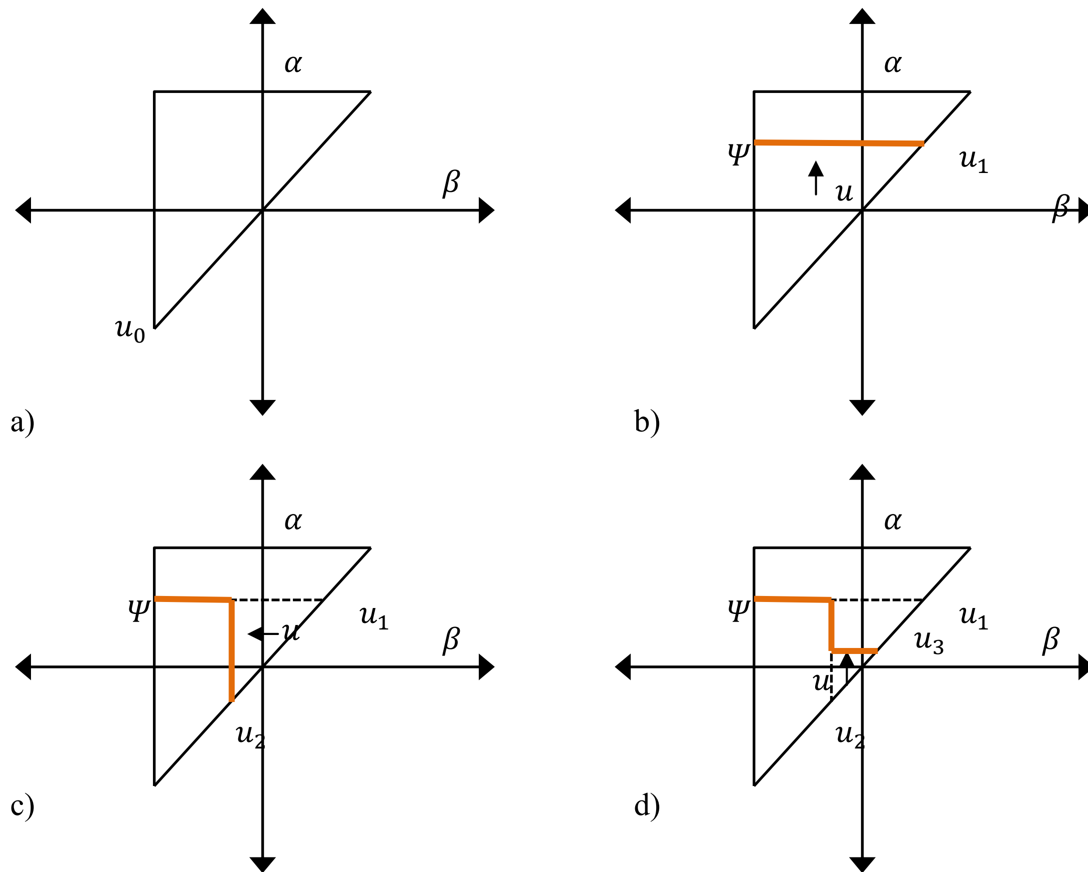

Figure A.3 – Preisach operator operational principle.

Figure A.4 shows a block diagram of the discrete Preisach operator model from figure A.2 which takes into account the weights μ of each hysteron [51]. Using a parameter identification scheme such as the least square method, experimental data output y and input u can be used to determine the weighting functions μ.

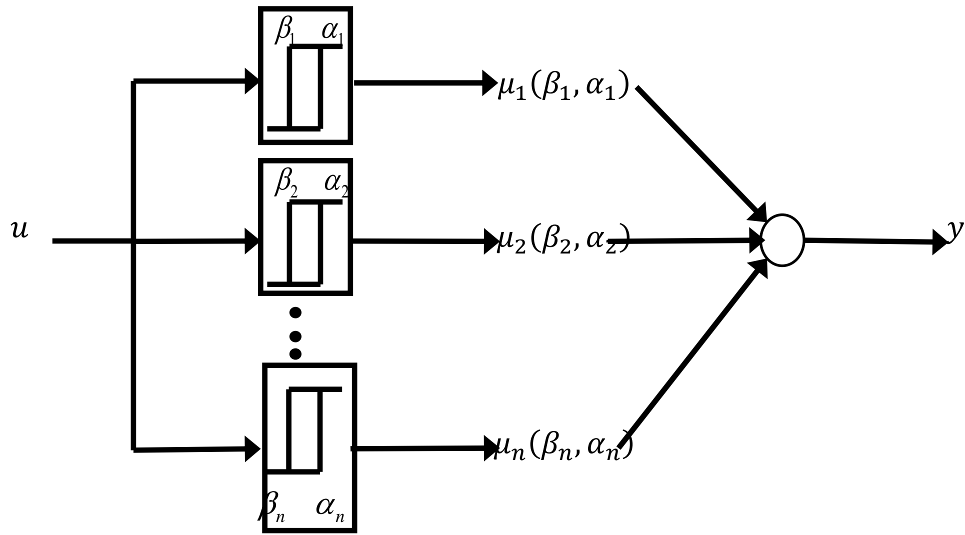

Figure A.4 – Discretized Preisach output block model with weighting functions.

A.2 The Inversion Problem

In order to approximately cancel the effects of hysteresis for control operations, an inverse scheme have been reported by [52] where adaptive control techniques were implemented in a hysteretic microactuator. In this model, shown in figure A.5, the inversion scheme W^{-1} and the hysteretic system W are connected in series. More general, the block diagram consists of four stages: 1. the inverse Preisach operator Γ^{-1} which estimates the inversion variable based on the measured variable y, 2. the algorithm that sends the signal to the system $I(x)$, 3. the system $G_0(I)$ which is controlled by $I(x)$, and 4. the Preisach operator. This configuration cancels the hysteresis and makes the system controllable with a simple

controller such as a PID. The adaptive algorithm used to calculate the inverse Preisach model has been studied by [53] with theoretical and experimental results.

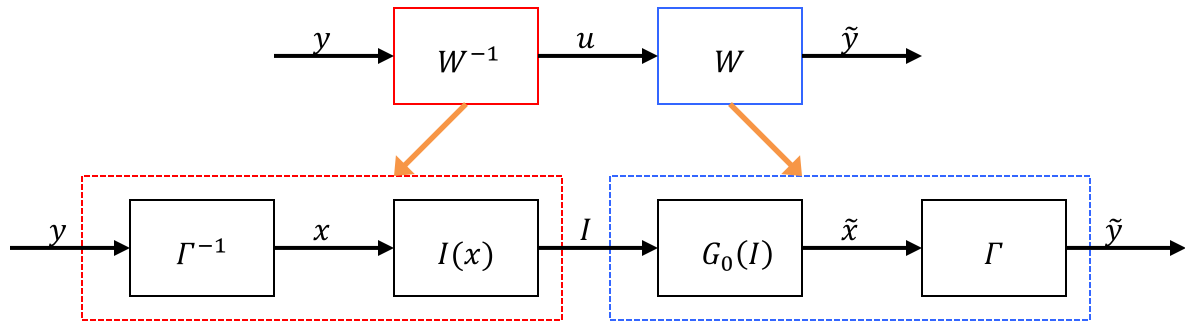

Figure A.5 – Inversion block diagram.

There are two methods for calculating the inverse Preisach operator: 1. the trajectory inversion problem which is solved by the closest match algorithm, and 2. the value inversion problem which is solved by solving the Preisach as a Finite State Machine (FSM) [53].

A.3 VO2 Modeling and Control

The Preisach operator theory is well suited for the modeling and control VO_2 actuators since its parameters can be obtained through experimental data manipulation. The first step towards VO_2 hysteresis control is to determine the rate dependency of VO_2. For systems operating at frequencies lower than 5 Hz, the hysteresis is rate independent, but as the frequency increases the shape of the hysteresis change. In the case of VO_2 MEMS devices, such as microbridges, the rate dependency for both actuation methods should be determined. Since the *conduction method* operates at frequencies much lower than 5 Hz, it is

expected that this will be rate independent. For the *irradiation method*, the frequencies of operation can reach much higher values than 5 Hz and the rate dependency of the system needs to be studied. After these rate dependence considerations, the second step is to determine a simple control experiment where the resistance of a VO_2 thin film will be controlled with a Peltier heater (expected rate independent).

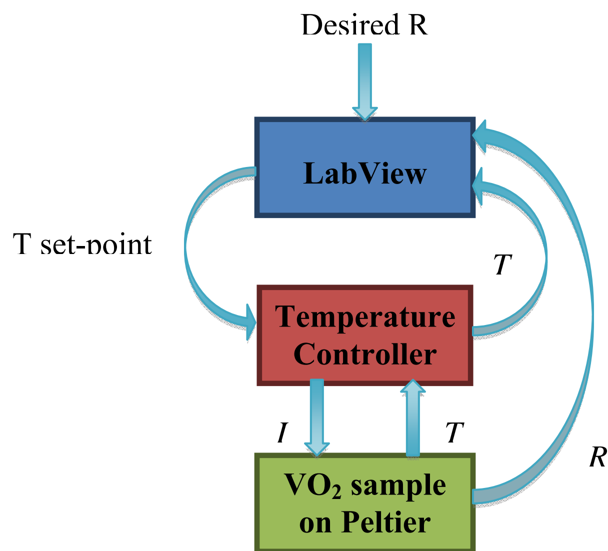

Figure A.6 – VO_2 resistance control scheme.

In this model *R* is the resistance, *T* is the temperature and *I* is the current supplied to the Peltier. *T* and *R* will be constantly measured by LabView which will calculate the set-point temperature based on the inverse operator and send it to the temperature controller. The controller will have a high precision control (0.1 ℃) and will control the sample's temperature in closed loop to produce a desired resistance value. This results in a rate independent model based on the following:

$$T(t) = c_0 I(t) ,$$
$$y(t) = R(t) = \Gamma[T(\cdot), \Psi_0](t) . \quad \text{(A.2)}$$

Using the theory on inverse Preisach operator, the dynamic model can be represented by the block diagram in figure A.7. The Preisach operator and its inverse will be calculated based on the theory discussed in the previous section and using experimental data. To get this data, a piecewise function, such as a triangular function, will be used as the input T and the corresponding values of R will be measured.

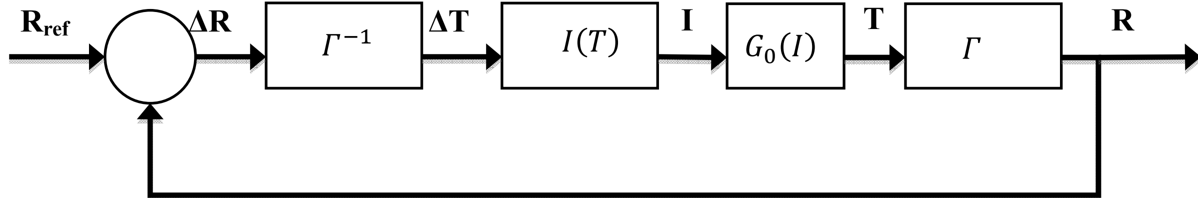

Figure A.7 – Block diagram of dynamic model for controlled VO_2 hysteresis.

After this control scheme is achieved the following approaches will be to:

1. Control the resonant frequency of VO_2-coated microbridges.
2. Control the displacement of VO_2-coated microcantilevers.
3. Use optical radiation to control VO_2 MEMS devices.
4. Control optical transmission through VO_2 thin film.

REFERENCES

[1] F. J. Morin, “Oxides Which Show a Metal-To-Insulator Transition at the Neel Temperature”. *Physical Review Letters*, 1959. **3**(1): pp. 34-36.

[2] G. A. Rozgonyi, D. H. Hensler, “Structural and Electrical Properties of Vanadium Dioxide Thin Films”. *The Journal of Vacuum Science and Technology*, 1968. **5**(6): pp. 194-199.

[3] A. Cavalleri, Cs. Tóth, C. Siders, J. A. Squier, F. Ráksi, P. Forget, J. C. Kieffer, “Femtosecond structural dynamics in VO_2 during an ultrafast solid-solid phase transition”. *American Vacuum Society*, 2004. **22**(3): pp. 859-864.

[4] B. G. Chae, H.T. Kim, D. H. Youn and K. Y. Kang, “Abrupt Metal-Insulator Transition Observed in VO_2 Thin Films Induced by a Switching Voltage Pulse”. *Physica B: Condensed Matter,* 2005. **369**(1): pp. 76-80.

[5] A. Perucchi, L. Baldassarre, E. Arcangeletti, D. Di Castro, P. Postorino, S. Lupi, “Infrared Study of Pressure-Induced Insulator to Metal Transitions in Vanadium Oxide Compounds at the SISSI@Elettra Beamline”. *Infrered Physics and Technology*, 2008. **51**(5): pp. 440-442.

[6] M. J. Dicken, K. Aydin, I. M. Pryce, L. A. Sweatlock, E. M. Boyd, S. Walavalkar, J. Ma and H. A. Atwater, “Frequency Tunable Near-Infrared Metamaterials Based on VO_2 Phase Transition”. *Optics Express*, 2009. **7**(20): pp. 18330-18339.

[7] J. Givernaud, C. Champeaux, A. Catherinot, A. Pothier, P. Blondy and A. Crunteanu, “Tunable Band Stop Filters Based on Metal-Insulator Transition in Vanadium Dioxide Thin Films”. *IEEE Microwave Symposium Digest*, 2008: p. 1103 – 1106.

[8] T. Driscoll, “Phase-Transition Driven Memristive System”. *Applied Physics Letters*, 2009. **95**(4): 043503.

[9] A. Rúa, F. Fernández and N. Sepúlveda, “Resonant Frequency Behavior of Silicon Cantilevers Coated with Nanostructured and Microcrystalline VO_2 Films”. *IEEE Transactions on Nanotechnology*, 2010. **9**(3).

[10] A. Rúa, F. Fernández, R. Cabrera and N. Sepúlveda, “Young’s Modulus of Pulsed-Laser Deposited V_6O_{13} Thin Films”. *Journal of Applied Physics*, 2009. **105**(11): 113504.

[11] G. S. Chung and J. M. Jeong, “Fabrication of micro heaters on polycrystalline 3C-SiC suspended membranes for gas sensors and their characteristics”. *Microelectronic Engineering*, 2010. **87**(11): pp. 2348-2352.

[12] M. Einat and M. Grajower, “Microboiling Measurements of Thermal-Inkjet Heaters”. *Journal of Microelectromechanical Systems,* 2010. **19**(2): pp. 391-395.

[13] P. Baum, D. S. Yang and A. Zewail, “4D Visualization of Transitional Structures in Phase Transformations by Electron Diffraction”. *Science*, 2007. **318**(788): pp. 788-792.

[14] M. M. Qazilbash, M. Brehm, B. G. Chae, P. C. Ho, G. O. Andreev, B. J. Kim, S. J. Yun, A. V. Balatsky, M. B. Maple, F. Keilmann, H. T. Kim and D. N. Basov, "Mott Transition in VO_2 Revealed by Infrared Spectroscopy and Nano-Imaging". *Science*, 2007. **318**(1750): pp. 1750-1753.

[15] A. Rúa, F. Fernández, M. Hines and N. Sepúlveda, "Study of the Resonant Frequencies of Silicon Microcantilevers Coated with Vanadium Dioxide Films During the Insulator-to-Metal Transition". *Journal of Applied Physics*, 2010. **107**(5): 053528.

[16] A. Rúa, F.E. Fernández, and N. Sepúlveda, "Bending in VO_2-coated microcantilevers suitable for thermally activated actuators". *Journal of Applied Physics*, 2010. **107**(7): 074506.

[17] N. Sepulveda, A. Rúa, R. Cabrera and F. Fernandez, "Young's Modulus of VO_2 Thin Films as a Function of Temperature Including Insulator-to-Metal Transition Regime". *Applied Physics Letters*, 2008. **92**(19): 191913.

[18] D. Bouyge, A. Crunteanu, J. Orlianges, D. Passerieux, C. Champeaux, A. Catherinot, A. Velez, J. Bonache, F. Martin and P. Blondy, "Reconfigurable Bandpass Filter Based on Split Ring Resonators and Vanadium Dioxide (VO_2) Microwave Switches". *Microwave Conference APMC* 2009.

[19] L. Chua, "Memristor- The Missing Circuit Element". *IEEE Transactions on Circuit Theory*, 1971. **18**(5): pp. 507-519.

[20] D. Strukov, G. Sneider, D. Steward and R. Williams, "The Missing Memristor Found". *Nature*, 2008. **453**: pp. 80-83.

[21] T. Driscoll, H. Kim, B. Chae, B. Kim, Y. Lee, N. Jokerst, S. Palit, D. Smith, M. Di Ventra and D. Basov, "Memory Metamaterials". *Science*, 2009. **325**(5947): pp. 1518-1521.

[22] L. Almeidal, G. S. Deep and A. Lima, "A Novel Preisach Operator for Modeling of Hysteresis in VO_2 Microbolometer". *IEEE Instrumentation and Measurement Technology Conference,* 2002: pp. 281-286.

[23] J. Dai, X. Wang, S. He, H. Ma, J. Lai and X. Yi, "Modeling of Hysteresis in Nanocrystalline VO_2 Thin Films with Random Resistor Networks". *IEEE International Conference on Nanotechnology*, 2007: pp. 1265-1268.

[24] S. D. Senturia, "Microsystem Design". pp. 235 and 413, 1st edition. Kluwer Academic Publishers, 2001.

[25] S. P. Timoshenko, D. H. Young and W. Weaver, "Vibration Problems in Engineering". Ch. 5, 4th edition. John Wiley and Sons, 1974.

[26] S. Bouwstra and B. Geijselaers, "On the Resonance Frequencies of Microbridges". *IEEE International Conference on Solid-State Sensors and Actuators*, 1991: pp. 538-542.

[27] A. H. Nayfeh and S. A. Emam, "Exact Solution and Stability of Postbuckling Configurations of Beams". *Nonlinear Dynamics*, 2008. **54**(4): pp. 395-408.

[28] D. R. Southworth, L. M. Bellan, Y. Linzon, H. G. Craighead and J. M. Parpia, "Stress-based Vapor Sensing Using Resonant Microbridges". *Applied Physics Letters*, 2010. **96**(16): pp. 163503.

[29] N. Lobontiu, "Dynamics of Microelectromechanical Systems", p. 101, 1st edition. Springer, 2007.

[30] L. Nicu and C. Bergaud, "Experimental and Theoretical Investigations on Nonlinear Resonances of Composite Buckled Microbridges". *Journal of Applied Physics*, 1999. **86**(10): 5835.

[31] G. Zhang, V. Chu and J. P. Conde, "Electrostatically Actuated Bilayer Polyimide-Based Microresonator". *Journal of Micromechanics and Microengineering*, 2007. 1**7**(4): pp. 797-803.

[32] P. Norton and J. Brandt, "Temperature Coefficient of Resistance for p- and n- Type Silicon". *Solid-State Electronics*, 1977. **21**(7): pp. 969-974.

[33] O. M. Suárez, "Computation of Interdiffusion Coefficients in Binary Isomorphous Metallic Systems". *Journal of Materials Education*, 2001. **23**(4): pp. 179-188.

[34] H. Coy, R. Cabrera, N. Sepúlveda and F. E. Fernández, "Opto-electronic and Full-Optical Multiple State Memory Response in Phase-Change Materials". *Journal of Applied Physics,* 2010. **108**(11): 113115.

[35] A. B. Yu, A. Q. Liu and Q. X. Zhang. "Tunable MEMS LC Resonator with Large Tuning Range". *Electronics Letters*, 2005. **41**(5): pp. 855-857.

[36] E. M. Prophet, J. Musolf, B. F. Zuck, S. Jimenez, K. E. Kihlstrom and B. A. Willemsen. "Highly-Selective Electronically-Tunable Cryogenic Filters Using Monolithic, Discretely-Switchable MEMS Capacitor Arrays". *IEEE Transactions in Applied Superconductivity*, 2005. **15**(2): pp. 956-959.

[37] B. Lakshminarayanan, D. Mercier and G. M. Rebeiz. "Highly-Reliable Miniature RF-MEMS Switched Capacitors". *IEEE Transactions on Microwave Theory and Techniques*, 2008. **56**(4): pp. 971-981.

[38] X. Liu, L. Katehi, W. J. Chappell and D. Peroulis, "High-Q Tunable Microwave Cavity Resonators and Filters Using SOI-Based RF MEMS Tuners". *Journal of Microelectromechanical Systems*, 2010. **19**(4): pp. 774-784.

[39] B. Morgan and R. Ghodssi, "Vertically-Shaped Tunable MEMS Resonators". *Journal of Microelectromechanical Systems*, 2008. **17**(1): pp. 85-92.

[40] T. Driscoll, J. Quinn, S. Klein, H. T. Kim, B. J. Kim, Y. V. Pershin, M. Di Ventra, and D. N. Basov, "Memristive Adaptive Filters". *Applied Physics Letters*, 2010. **97**(9): 093502.

[41] E. Merced, R. Cabrera, R. Suarez, F. E. Fernández and N. Sepúlveda, "Nanostructured VO2 Film Coatings for Tunable MEMS Resonators", *Nanotechnology Material and Devices Conference (NMDC),* 2010: pp. 212-215.

[42] W. C. Young and R. G. Budynas*, "*Roark's Formulas for Stress and Strain McGraw-Hill"*,* 7th edition. McGraw-Hill, pp. 137, 2002.

[43] M. Guntersdorfer, "Conductivity Anomaly in Vanadium Dioxide". *Solid-State Electronics,* 1970. **13**(355).

[44] P. Jin, S. Nakao, S. Tanemura, T. Bell, L.S. Wielunski and M.V. Swain, "Characterization of Mechanical Properties of VO2 Thin Films on Sapphire and Silicon by Ultra-Microindentation". *Thin Solid Films*, 1999. **343-344**: pp. 134-137.

[45] K. Y. Tsai, T. S. Chin, and H. P. Shieh, "Effect of Grain Curvature on Nano-Indentation Measurements of Thin Films". *Japan Journal of Applied Physics*, 2004. **43**(9): pp. 6268-6273.

[46] D. Kucharczyk and Z. Niklewski, "Accurate X-ray Determination of the Lattice Parameters and the Thermal Expansion Coefficients of VO2 Near the Transition Temperature". *Journal of Applied Crystallography*, 1979. **12**: pp. 370-373.

[47] D. W. Oh, C. Ko, S. Ramanathan and D.G. Cahill, "Thermal Conductivity and Dynamic Heat Capacity Across the Metal-Insulator Transition in thin film VO_2". *Applied Physics Letters*, 2010. **96**(15): 151906.

[48] C. N. Berglund and H. J. Guggenheim, "Electronic Properties of VO_2 near the Semiconductor-Metal Transition". *Physical Review*, 1969. **185**(3): pp. 1022-1033.

[49] Y. Jiazhen, Z. Yue, H. Wanxia, T. Mingjin, "Effect of Mo-W Co-doping on Semiconductor-Metal Phase Transition Temperature of Vanadium Dioxide Film". *Thin Solid Films*, 2008. **516**(23): 8554-8558.

[50] B. Chen, D. Yang, P. A. Charpentier, M. Zeman, "Al^{3+}-doped Vanadium Dioxide Thin Films Deposited by PLD". *Solar Energy Materials and Solar Cells*, 2009. **93**(9): pp. 1550-1554.

[51] I. Mayergoyz, "Mathematical Models of Hysteresis and Their Applications", 1st edition. Elsevier.

[52] R. Venkatamaran, "Modeling and Adaptive Control of Magnetostrictive Actuators". PhD Thesis, University of Maryland, College Park, 1999.

[53] X. Tan, J. S. Baras, P. S. Krishnaprasad, "Control of Hysteresis in Smart Actuators with Application to Micropositioning". *Systems and Control Letters*, 2005. **54**(5): pp. 483-492.